Native defects in bulk and monolayer MoS_2 from first principles

Hannu-Pekka Komsa[1] and Arkady V. Krasheninnikov[2]
[1]*COMP, Department of Applied Physics, Aalto University, P.O. Box 1100, 00076 Aalto, Finland*
[2]*Department of Applied Physics, Aalto University, P.O. Box 1100, 00076 Aalto, Finland*
(Received 23 December 2014; revised manuscript received 26 February 2015; published 12 March 2015)

We present an extensive first-principles study of a large set of native defects in MoS_2 in order to find out the types and concentrations of the most important defects in this system. The calculations are carried out for both bulk and monolayer forms of MoS_2, which allows us to study how defect properties change between these two limiting cases. We consider single- and few-atom vacancies, antisites, adatoms on monolayer, and interstitials between layers in the bulk material. We calculate the formation energies of neutral and charged defects, determine the charge transition levels, and from these self-consistently assess the concentration of defects at thermal equilibrium as well as the resulting positions of the Fermi level. The chemical potential values corresponding to different growth conditions are carefully accounted for, and for all values of chemical potentials relevant to the growth of MoS_2, the S vacancies are found to be the most abundant defects. However, they are acceptors and cannot be the cause of the often observed n-type doping. At the same time, Re impurities, which are often present in natural MoS_2 samples, naturally provide good n-type doping behavior. We also calculate migration barriers for adatoms and interstitials and discuss how they can affect the growth process.

DOI: 10.1103/PhysRevB.91.125304 PACS number(s): 31.15.es, 61.72.J−, 73.20.Hb

I. INTRODUCTION

Transition-metal dichalcogenides (TMDs), along with other two-dimensional (2D) materials, are currently under intense scrutiny due to their unique properties [1,2]. The prototypical TMD material is molybdenum disulfide (MoS_2), which is abundant in nature and cheap. Monolayers of MoS_2, which can be grown on a suitable substrate or exfoliated from the bulk material, show extraordinary optical [3–5], electrical [6], and mechanical properties [7,8]. As a result, MoS_2 (and other TMDs) hold great promise for future optoelectronic [6,9], catalytic [10,11], and sensing [12] applications.

Bulk MoS_2 can also be prepared in a multitude of ways, such as vacuum heating of molybdenum trisulfide and reacting molybdenum or molybdenum trioxide with sulfur or hydrogen sulfide [13]. High-quality crystalline samples can be obtained by chemical vapor transport (CVT) process [14,15]. Similar techniques have been previously used to grow MoS_2 nanotubes and fullerenelike structures [16–18]. Recently, the focus has shifted to ultrathin, down to monolayer-thick, structures. These are manufactured by sulfurization of thin molybdenum layers [11,19–22], CVT- and chemical vapor deposition (CVD)-type approaches [11,21,23–25], or other means [26–28]. Some of these approaches give large areas of MoS_2 with good crystalline quality and uniform thickness, whereas others may be more suited for production of small nanoparticles [29,30].

As any other material, TMDs have defects, which are essential in determining electrical [31–34], magnetic [35], and optical properties [36,37]. Moreover, defects in a material with reduced dimensionality are expected to have a much stronger impact on its electronic properties, as compared to its bulk counterpart. During the material growth, often occurring at relatively high temperatures, native defects are inevitably introduced. The equilibrium concentrations are determined by the growth conditions (pressure, temperature, and the abundance of constituents) and the defect formation energies. After the cooling of the sample, some of the defects remain in the lattice. Furthermore, defects may be formed later on in the processing stages.

Often high-quality crystalline samples with small concentration of defects are desirable for applications. The types and concentrations of defects have to be known before they can be controlled. Unfortunately, quantifying defect concentrations is difficult in practice. For instance, a scanning tunneling microscope (STM) probes only the surface and energetic electrons of the beam in a transmission electron microscope (TEM) may damage the sample [38,39]. Consequently, the concentrations of defects observed in different experiments vary strongly depending on the details of the experiments [32,38–44], and thus better understanding of the origin of these defects is required.

In addition to the native defects unintentionally introduced during growth, defects may also be produced deliberately at the postgrowth stage. This can be achieved by electron irradiation [38,45], ion bombardment [37,46–52], chemical treatment such as selenization [53], plasma treatment [54], STM voltage pulsing [55,56], or vacuum annealing [32,37,57–59]. Such processes are useful as they allow controlled modification of the material properties after the growth.

Finally, there is still uncertainty about the origin of the often observed n-type doping of MoS_2, which depends on the sample and environment [34,60,61]. Natural samples often contain Re impurities, which are shallow donors. There is no Re in synthetic samples, but there can still be plenty of S vacancies, which have then also been assigned as the source of n-type doping [32,62,63]. On the other hand, in the studies of 2D samples, the charge transfer with the substrate, and the environment in general, will play a significant role [60].

To address these issues, we have studied a large set of native defects in bulk and monolayer MoS_2 using density functional theory calculations. In spite of several previous works on the topic, a systematic study has not yet been carried out. We consider Mo and S vacancies, antisites, adatoms on monolayer, and interstitials in bulk. We have calculated formation energies of neutral and charged defects, which allows us to determine

 ©2015 American Physical Society

the thermodynamical charge transition levels. In addition, we consider the role of Re doping, a common extrinsic impurity. With all this information at hand, we determine thermal equilibrium defect concentrations and Fermi-level positions as functions of temperature and S partial pressure. We also examine the diffusion of adatoms and interstitials in these systems.

The paper is organized as follows. In addition to basic computational parameters, an in-depth description of proper choices of chemical potentials and the finite-size supercell correction methods for charged defects are given in Sec. II. Basic structural and electronic properties of all considered defects, together with their formation energies, are briefly described in Sec. III. In addition, alignment of charge transition level positions and diffusion properties of adatoms and interstitial atoms are discussed at the end of Sec. III. Calculations for defect concentrations and Fermi-level positions at thermal equilibrium under different growth conditions are reported in Sec. IV. The conclusions are drawn in Sec. V.

II. METHODS

A. Basic parameters

Our density functional theory (DFT) calculations are carried out using the plane-wave basis and projector augmented plane wave (PAW) description of the core regions, as implemented in the VASP package [64,65]. We adopt plane-wave cut off of 500 eV, which yields total energies converged within 1 meV/atom. Description of the exchange correlation is built on top of the Perdew-Burke-Ernzerhof (PBE) functional [66]. The Van der Waals interactions are treated via the empirical correction proposed by Grimme (PBE-D) [67], which gives the structural parameters in good agreement with experimental values as well as with the random phase approximation calculations (RPA) [68,69]. PBE and PBE-D give very similar defect geometries and energies. However, to make sure that the binding energy between the layers, and thus the rigidity of the environment, is properly accounted for in the case of Mo and S interstitials in bulk MoS_2, the calculations are carried out at the PBE-D level. During ionic relaxation, the convergence criterion for forces is set to 10 meV/Å.

In selected cases, we also carry out hybrid functional calculations, relying on the form proposed by Heyd, Scuseria, and Ernzerhof (HSE06) [70,71]. Hybrid functionals open the band gap and appear to also lead to better defect level positions within the gap in good agreement with the experiment [72,73] and higher level of theory [74], as well as to yield total formation energies that are in good agreement with the RPA calculations [75]. In addition, due to decreased self-interaction error, in partially occupied degenerate state systems hybrid functionals often lead to qualitatively correct electron/hole localization around the defect unlike the semilocal functionals. In these calculations, the Fock integral over the Brillouin zone is sampled at a halved grid.

The bulk parameters using the two adopted functionals are collected in Table I. The k-point sampling of $12 \times 12 \times 1$ and $12 \times 12 \times 4$ for monolayer and bulk, respectively, was found to yield total energies converged well within 1 meV/atom. The band gaps are calculated without spin-orbit coupling. It can be seen that both lattice parameters are already rather well reproduced by the PBE-D functional. HSE gives a better in-plane lattice constant but fails in reproducing the interlayer distance due to missing van der Waals interaction and thus the out-of-plane lattice constant is here fixed to the experimental value. The dielectric constants in both directions are in very good agreement with the experiments. The bulk band gap calculated with HSE is about 0.3 eV larger than the experimental one, whereas the PBE-D band gap is underestimated by the same amount. Comparison to the experiment in the case of monolayer is more complicated. The dominant optical gap measured at low temperature is 1.95 eV [5,82]. The exciton binding energy are experimentally found to lie between 0.3 and 0.7 eV in all TMDs [63,83–88]. The spread of the results is likely related to the dielectric environment in which the experiments were performed [88,89]. The exciton binding energy is calculated to be 0.5–0.6 eV [90,91], which yields a fundamental gap of 2.5 eV.

TABLE I. Basic material properties for MoS_2 calculated with PBE-D and HSE functionals together with the experimental values: in-plane lattice constants a (in Å), ratio between the out-of-plane and in-plane lattice constants c/a, band gaps for monolayer and bulk E_g (in eV), and in-plane $\varepsilon_{||}$ and out-of-plane $\varepsilon_{\perp}$ dielectric constants for bulk (high-frequency value plus ionic contribution). Experimental values for lattice constants and dielectric constants are from Refs. [76,77], for bulk band gaps from Refs. [78–81], and for monolayer band gaps from Refs. [5,82].

	a	c/a	E_g^{ML}	E_g^{bulk}	$\varepsilon_{\parallel}$	$\varepsilon_{\perp}$
PBE-D	3.18	3.91	1.69	0.95	15.11 + 0.18	6.13 + 0.04
HSE	3.16	3.89	2.21	1.47		
Expt.	3.16	3.89	1.95/2.5	1.2	15.2	6.2

PBE-D clearly underestimates even the optical gap. The HSE band gap appears to fall between the optical and fundamental gaps, but should be more in line with experiment, since, as mentioned, the fundamental gap decreases when the dielectric constant of the environment increases.

B. Defect formation energies

The defective systems are modeled with 6×6 supercell for monolayer MoS_2 and $c = 6a$ (i.e., about 19-Å interlayer separation). For bulk MoS_2, we employ $5 \times 5 \times 1$ supercell, where the c lattice constant is tilted ($c^0 + 2a^0 + 2b^0$, where a^0, b^0, and c^0 are the primitive cell lattice vectors). This improves the convergence of total energies with respect to cell size, since the bulging of layers caused by the interstitial atoms do not coincide in the perpendicular direction. The adopted k-point samplings are $2 \times 2 \times 1$ and $2 \times 2 \times 2$ for monolayer and bulk, respectively. In the initial atomic configuration of defect calculations, the symmetry of the crystal was broken by adding random displacements to all ions.

For the calculation of defect concentrations and formation energies we follow the standard approach as described in Refs. [92–95]. The concentration of the defects at thermal equilibrium can be calculated from the Gibbs free energy of

defect formation G_f as

$$c = N_0 N_c \exp\left(-\frac{G_f}{k_B T}\right), \quad (1)$$

where N_0 is the number of sites (MoS_2 primitive cells) per unit volume and N_c is the number of inequivalent configurations.

G_f for a defect in charge state q is defined as

$$G_f = F(\mathrm{def}) - F(\mathrm{host}) + pV_f - \sum_i n_i \mu_i + q(E_v + E_F) + E_{\mathrm{corr}}, \quad (2)$$

where $F(\mathrm{def})$ and $F(\mathrm{host})$ are the Helmholtz free energies of the system with and without the defect, p is pressure and V_f is the formation volume of the defect, which is here assumed to be zero for simplicity as the concept becomes somewhat poorly defined in the case of monolayer materials. μ_i are chemical potentials of the removed or added atoms and n_i are their numbers. E_v is the valence band maximum and E_F is the Fermi-level position with respect to E_v. Spurious interactions between images of the defects within the periodic supercell approach are corrected for with the E_{corr} term [96].

The free energy of the system can be written as

$$F = F^{\mathrm{el}} + F^{\mathrm{qh}} + F^{\mathrm{ah}}, \quad (3)$$

where F^{el} is the electronic free energy and F^{qh} and F^{ah} are the quasiharmonic and anharmonic contributions to the free energy from lattice vibrations, respectively. At 0 K, $F^{\mathrm{el}} = E_0$, where E_0 is the total energy from DFT at 0 K electronic temperature. It can be argued that when taking the free energy difference in Eq. (2), much of the vibrational contributions from the two supercell calculations cancel out. As shown in Appendix B, the harmonic contributions tend to be within 0.2 eV. Furthermore, due to the large gap between occupied and unoccupied states, the finite temperature effects on the electronic subsystem are small and thus we generally use $F = E_0$. Only for the most important case of S vacancy are the lattice vibrations accounted for as discussed in Sec. IV.

We next search for realistic physical limits for the chemical potentials needed in Eq. (2). When considering the elemental phases, the chemical potential is simply proportional to the Gibbs energy of the system $\mu = \partial G/\partial N = G/N$. The total Gibbs energy at temperature T and at reference pressure p^0 can be written as

$$G = H - TS = E(T=0) + E^{\mathrm{vib}} + \Delta H(T,p^0) - T\Delta S(T,p^0), \quad (4)$$

where E is the internal energy, E^{vib} is the energy of the zero-point vibrations, ΔH accounts for the changes in enthalpy when going from $T = 0$ to a finite T, and, correspondingly, S accounts for the changes in entropy. E and E^{vib} are obtained from DFT calculations. At the standard pressure of $p^0 = 100$ kPa, ΔH and ΔS can be easily obtained from thermochemical tables [97,98]. We assume this is always the case for the solid phases. For gases, the chemical potential at pressure p can be easily obtained if we assume ideal gas behavior:

$$\mu(T,p) = \mu(T,p^0) + \int_{p^0}^{p} \frac{\partial G}{\partial p} dp = \mu(T,p^0) + kT \ln\left(\frac{p}{p^0}\right). \quad (5)$$

In the present study, we first assume that the chemical potential of Mo and S are in a thermal equilibrium with MoS_2,

$$\mu_{\mathrm{MoS_2}} = \mu_{\mathrm{Mo}} + 2\mu_{\mathrm{S}}. \quad (6)$$

The accessible range of μ_{Mo} and μ_{S} values is further limited by the lowest energy phases of these elements. Nowadays, good quality materials are often grown by CVD method [11,15,21,23–25], where the temperatures of the growth zone vary between 650° C and 950° C. Thus, the assumption of thermal equilibrium should be reasonably valid.

Hydrogen may or may not be abundantly present during the growth. In the early investigations of the edge structures of MoS_2 under conditions relevant for hydrodesulfurization process [99,100], the sulfur was in balance with H_2S and thereby μ_{S} was determined by hydrogen pressure. However, many of the growth methods mentioned above do not contain appreciable amounts of hydrogen and therefore we take the sulfur chemical potential from the elemental phase.

Choosing the value of sulfur chemical potential is somewhat complicated by the large number of S allotropes. Below 100° C, sulfur is solid in the α-S allotrope consisting of loosely bound S_8 rings. Above 120°C S is in the liquid phase, above 720°C S is a gas consisting of various S molecules, and above 880°C it is found as diatomic S_2 gas [97]. At typical CVD growth temperatures, which tend to be above 700° C, elemental S is thus in gaseous phase.

For the S_2 gas, the chemical potential depends on the temperature and on partial pressure. Using Eqs. (4) and (5), the full formula for S_2 chemical potential becomes [93,101]

$$\mu_{\mathrm{S}}(T,p) = \frac{1}{2}\mu_{\mathrm{S_2}} = \frac{1}{2}\left[E_{\mathrm{S_2}} + E^{\mathrm{vib}}_{\mathrm{S_2}}(0\ \mathrm{K}) + \Delta H(T,p^0) - T\Delta S(T,p^0) + k_B T \ln\left(\frac{p_{\mathrm{S_2}}}{p^0}\right)\right]. \quad (7)$$

$E_{\mathrm{S_2}}$ is the calculated energy of an isolated S_2 molecule and $E^{\mathrm{vib}}_{\mathrm{S_2}}(0\ \mathrm{K})$ corresponds to vibrational energy due to the zero-point motion, also obtained from the calculations. Both the change in enthalpy and the change in the entropy of S_2 are extracted from the thermochemical tables [97,98] at $p^0 = 100$ kPa or 1 bar.

For the solid phases of α-S, Mo, and Re we (i) neglect the pressure dependence, (ii) calculate the energy of zero-point vibrations, and (iii) extract the enthalpy and entropy contributions from the thermochemical tables. The free energy contributions are not available for Re or ReS_2 in the thermochemical tables and are thus estimated computationally using the PHON program [102]. The force matrix is calculated using a $4 \times 4 \times 4$ supercell. We note that Mo (and Re) remain crystalline for all realistic growth temperatures. The Re and ReS_2 data were found to be very close to those of Mo and MoS_2, respectively.

The S chemical potential limits are shown in Fig. 1(a). The allowed range of μ_{S} chemical potentials is bounded by the S-rich limit above and Mo-rich limit below. In the S-rich limit we show both the tabulated reference curve that always follows the lowest energy phase [97] and the S_2 curves for different partial pressures. The situation for Mo is the opposite, as shown in Fig. 1(b). For example, if μ_{S} in MoS_2 is above the S-rich limit, then S will desorb to

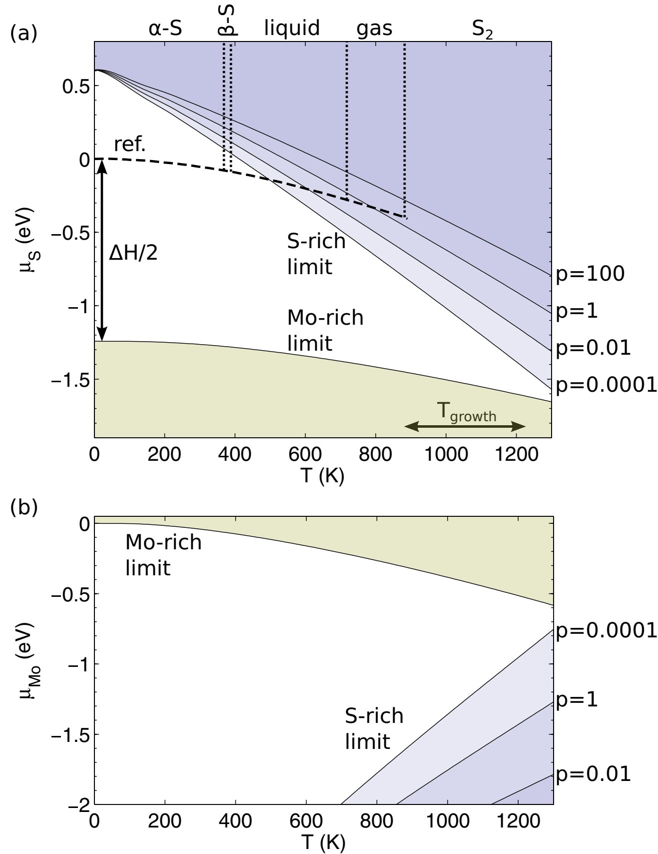

FIG. 1. (Color online) The limits of accessible (a) μ_S and (b) μ_{Mo} as a function of temperature while maintaining the equilibrium with MoS_2 [Eq. (6)]. In (a), the S-rich limit corresponds to different elemental S phases (either S_2 for few different pressures or the reference curve which always follows the lowest energy phase) and the Mo-rich limit to $\mu_S = (\mu_{MoS_2} - \mu_{Mo,bulk})/2$. In (b), the Mo-rich limit corresponds to $\mu_{Mo,bulk}$ and the S-rich limit to $\mu_{Mo} = \mu_{MoS_2} - 2\mu_{S,S2}$.

form this elemental phase. On the other hand, if μ_S is very low, then the balance with MoS_2 leads to μ_{Mo} above the Mo-rich limit, which will lead to Mo precipitate formation. The accessible range of chemical potentials is governed by the formation enthalpy $\Delta H = \mu_{MoS_2} - \mu_{Mo}^{max} - 2\mu_S^{max}$, for which we obtain 2.48 and 2.42 eV at 0 K and 300 K, respectively, in excellent agreement with the experimental value 2.44 eV at room temperature [103]. Moving on to higher temperatures, μ_S chemical potential at both limits decreases. Clearly then, $\mu_S = \mu_S(T = 0\,\text{K}, p^0)$ at the S-rich limit is not a proper choice when studying defect concentrations at growth temperatures. Furthermore, the S pressure can have a rather large effect on the chemical potential.

Finally, as we consider Re-doped samples, the chemical potential of Re has to be defined. There are two relevant choices: bulk phase of Re and ReS_2. For the latter, thermal equilibrium with ReS_2 again gives

$$\mu_{ReS_2} = \mu_{Re} + 2\mu_S, \tag{8}$$

where μ_S can change within the limits discussed above. The μ_{Re} values calculated from these two phases are shown in

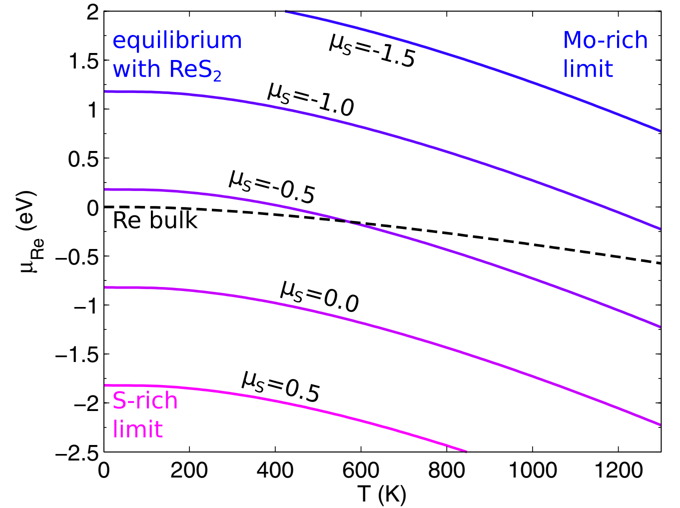

FIG. 2. (Color online) Temperature dependence of Re chemical potential μ_{Re} as obtained from bulk Re and from equilibrium with ReS_2 at different values of μ_S, which can be related to experimental conditions using Fig. 1. The energy zero is set to bulk Re at 0 K.

Fig. 2. In the Mo-rich limit at 0 K, Re bulk is lower in energy by 1.66 eV. For this value of μ_S, ReS_2 and bulk Mo would transform to bulk Re and MoS_2 phases. In the S-rich limit at 0 K (bulk S, $\mu_S = 0$), the balance with ReS_2 gives lower energy by −0.82 eV. At higher temperatures, the competition between the phases depends on a partial pressure of S. In this paper we always adopt the minimum value for μ_{Re} depending on the conditions.

C. Charged defects

Charged defect calculations employing supercell geometry with periodic boundary conditions are subject to spurious electrostatic interactions with the defect images over the supercell as well as with the background charge which is required to make the total system charge zero. In the context of 3D bulk materials, this issue has been widely studied and, consequently, several schemes for correcting the induced errors have been proposed [96,104–107]. These schemes should also be valid for layered bulk materials as long as the large anisotropy in the dielectric constant is accounted for. The correction scheme proposed by Freysoldt, Neugebauer, and Van de Walle (FNV) [106] only involves solving the Poisson equation, which is numerically straightforward even in the case of anisotropic dielectric constant. The alignmentlike term is taken from planar-averaged potential in the direction parallel to the MoS_2 sheet. We also test the applicability of a Madelung (or Makov-Payne) correction generalized to the anisotropic dielectric constant [108]. For both methods, we use the dielectric constants listed in Table I. As shown in Fig. 3(c), the FNV scheme appears to work very well, yielding consistently formation energy of about 2.3 eV, which is also in agreement with extrapolation from $4 \times 4 \times 1$ and $8 \times 8 \times 2$ supercells. The Madelung correction performs also reasonably well, slightly underestimating the correction: about 50 meV in the case of the $5 \times 5 \times 1$ supercell. These findings are in agreement with the benchmarks in Ref. [109] for anisotropic

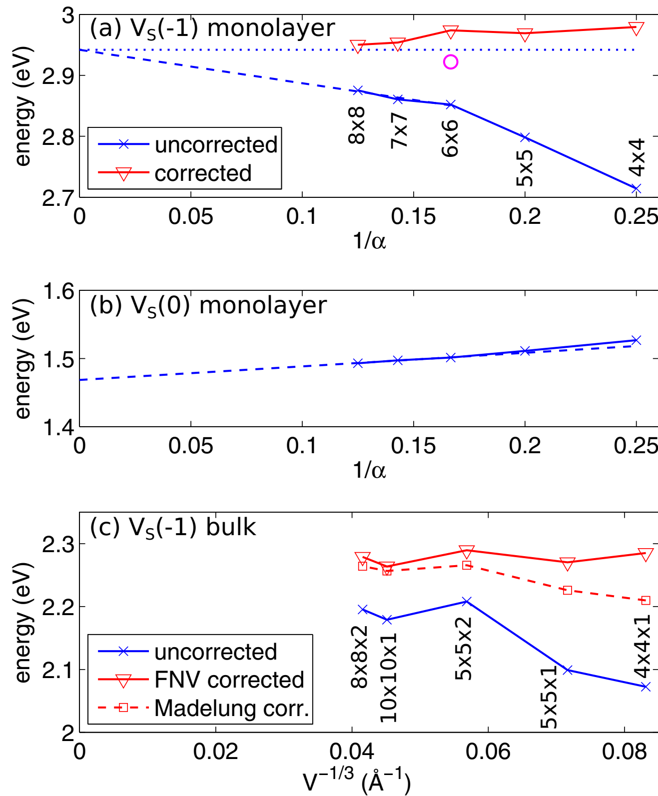

FIG. 3. (Color online) The formation energies of $V_S(-1)$ defect calculated at different supercell sizes in (a) monolayer and (c) bulk MoS_2. (b) Formation energy for the neutral V_S in monolayer MoS_2. The formation energies are shown with and without the electrostatic correction [E_{corr} in Eq. (2)]. In (a),(b), the supercell sizes are described by parameter α: $\alpha \times \alpha$ supercell with $c = \alpha a$. Using the three largest supercells, we extrapolate to infinite system size (dashed line). The circle (magenta) in (a) corresponds to the results obtained using the special vacuum, as described in Ref. [110].

materials. Due to the small difference in the formation energy, we applied the simpler Madelung correction.

In the case of monolayers, the situation is more complicated. The inhomogeneity of the dielectric environment needs to be included in the correction. A generalization of the bulk schemes to low-dimensional systems was recently introduced in Refs. [107,110] and successfully applied to MoS_2 in Refs. [111,112]. The quality of the correction is demonstrated in Fig. 3(a), where we show the uncorrected and corrected formation energy of the $V_S(-1)$ defect for a few different supercell sizes. The corrected energy Fig. 3(a) corresponds to carrying out the full procedure described in Ref. [110]. However, it was also suggested that in the case of a 6×6 supercell with a “special vacuum” of $c = 18$ Å, the correction would be about $q^2 \times 70$ meV. Here we have almost the same, $c = 19$ Å, and thus this correction should work well also in our case, which is indeed the case as shown in Fig. 3(a) by the circle (magenta). This is the correction that is adopted throughout the rest of this paper.

Finally, the thermodynamic charge transition levels are obtained from the position of Fermi level where the charge state changes. They are customarily given with respect to the valence band maximum (VBM) or the conduction band

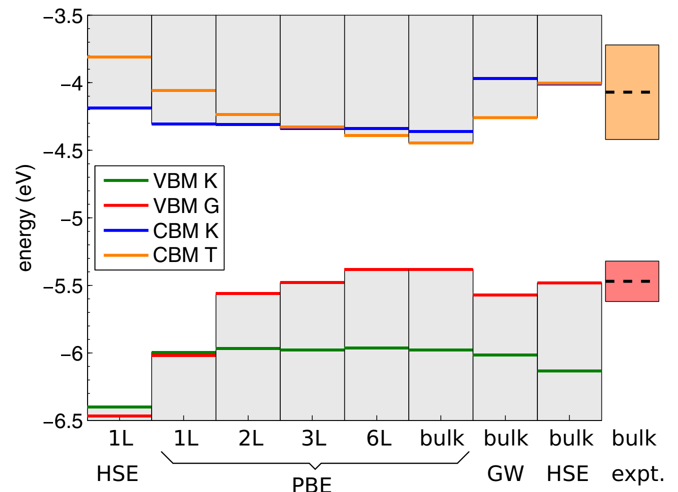

FIG. 4. (Color online) Valence and conduction band edge positions with respect to vacuum level as calculated using different levels of theory and different number of MoS_2 layers. The highest energy valleys of the valence band are located at K and Γ, and the lowest energy valleys of the conduction band at K and T (about half-way between Γ and K). Experimental values are from Ref. [118].

minimum (CBM). Correctly positioning the charge transition levels with the gap is difficult if the band gap is not correct in the calculation [113–116]. The problem is here accentuated by fact that the band edge positions depend heavily on the number of layers and the environment in which the thin film is embedded [89,117]. However, charge transition levels with respect to common energy reference are known to be a rigid quantity within the DFT scheme [74,113,114]. In 2D materials, vacuum level provides a natural well-defined energy reference. For the bulk system, we employ the standard approach of aligning the bulk band edges to vacuum through the electrostatic potential profile obtained from a few-layer slab calculation. Band edges obtained from one- to few-layer systems and the bulk system, at various levels of theory, are shown in Fig. 4. The experimental values are from Ref. [118]. More recently the monolayer has been reported to have ionization energy and electron affinity of 5.95 and 4.12 eV (1.83-eV band gap) on gold [119], respectively, and 5.90 and 3.56 eV (2.34-eV band gap) on Si [120].

The PBE(-D) results demonstrate the changes of the band edge positions as a function of the number of layers. The band edges at the K point are hardly affected, but the Γ- and T-point edges shift strongly due to the interlayer interactions, which is also the reason for the direct-indirect transition of the gap. The GW results for the bulk system appear to be in a good agreement with the experiment. Unfortunately, for monolayer, the band gap and thus the band edge positions depend strongly on the environment and are thus excluded here. It is worth noting that when the HSE functional is used, although the bulk band gap is clearly smaller than that of a monolayer, the CBM for bulk is 0.18 eV higher in energy than for monolayer. In any case, HSE also appears to reproduce the band edge positions reasonably well, although admittedly the experimental error bars are large.

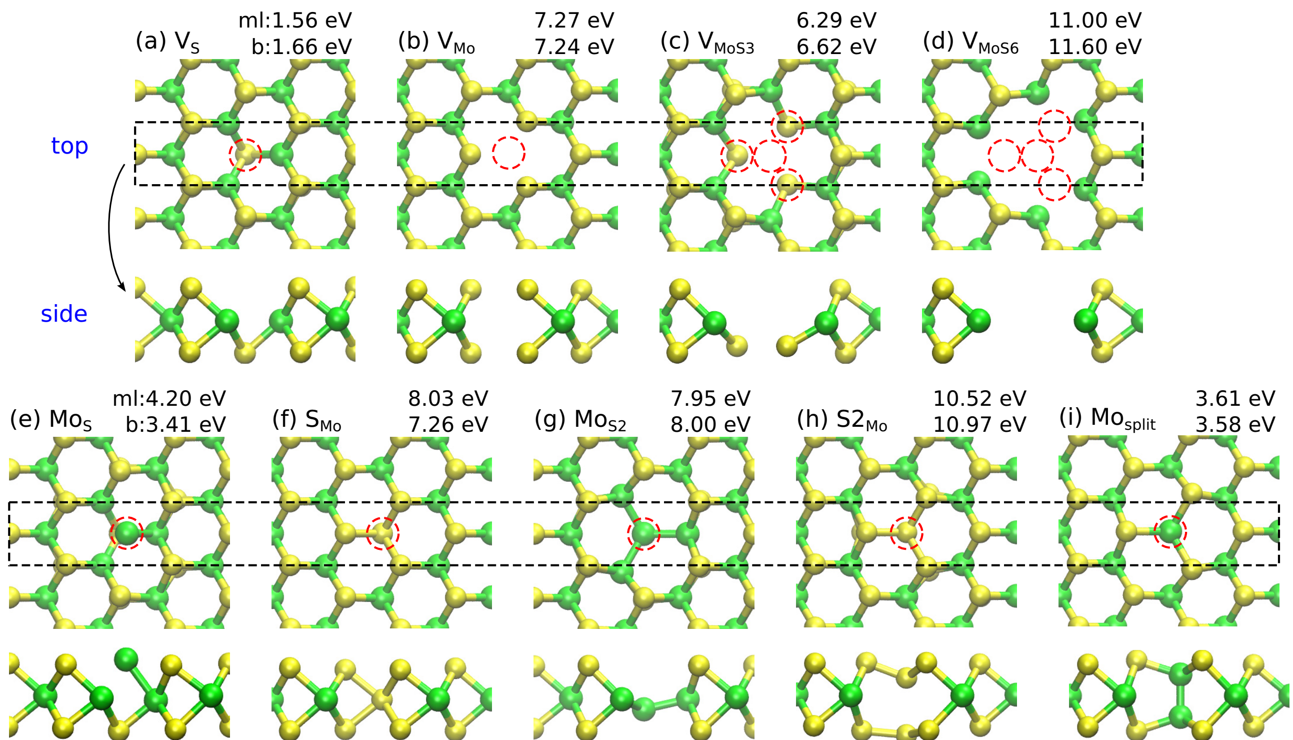

FIG. 5. (Color online) Final optimized geometries of the defects within a MoS_2 layer: vacancies (a)–(d), antisites (e)–(h), and the Mo-Mo split interstitial (i). Dashed circles (red) denote the position of the defect. The monolayer (ml) and bulk (b) formation energies in the neutral state are also given.

When reporting our computational results, the Fermi level and the band edges are given with respect to the vacuum level. This allows for easier alignment of the results with the edges for a different number of layers or when more accurate (experimental or computational) band edge positions become available.

III. BASIC DEFECT PROPERTIES

We start the discussion of the results by describing the basic geometries and the formation energies of all the candidate defects. The defects are divided into two groups depending on whether they are located inside the layer (vacancies and antisites) or outside the layer (adatoms and interstitials). Both the monolayer and bulk instances are considered. In the cases where the defects are located inside the layers, the defect geometries are very similar in the monolayer and bulk, and thus only the geometry for the monolayer is shown.

A good discussion of the electronic structure of vacancies and adatoms in monolayer MoS_2 can be found in Ref. [112] (additionally, cf. Refs. [39,121,122]). Here we only briefly touch on the electronic structure and focus on finding the energetically favored configurations.

A. Sulfur vacancy

The presence of a significant number of S vacancies in MoS_2 has been realized before. They have been observed directly by high-resolution transmission electron microscopy [32,38,39] and inferred by indirect means such as chemical reactions and x-ray photoelectron spectroscopy [37,40,46,58]. Motivated by these reports, several computational studies of S vacancy in MoS_2 have also been carried out [32,38,39,112,121,123–125]. In addition, clustering of the vacancies has been studied both experimentally and computationally [126–128].

The geometry of the S vacancy is shown in Fig. 5(a). The positions of the atoms surrounding the vacancy have changed only marginally from the pristine lattice positions. After the relaxation, the defect retains its "ideal" C_{3v} symmetry.

The formation energies of all defects as a function of the S chemical potential are shown in Fig. 6 in the neutral charge state. For a wide range of μ_S values, V_S has the lowest formation energy both in the monolayer and in the bulk. In fact, the S vacancy behaves very similarly both in the monolayer and in the bulk, and, unless otherwise noted, the discussion below holds for both cases.

The electronic structure is dominated by doubly degenerate unoccupied states deep within the band gap. Additionally, there is an occupied state lying very close to the VBM [32,38,39,112,121,123–125]. In the case of monolayer, we found this state to lie slightly below the VBM at the K point. The electronic structure of the neutral defect then suggests that the unoccupied states may accept from one to few electrons and the low-lying occupied state may be able to donate one electron.

Graphs of formation energy vs Fermi-level position, as calculated with PBE-D, are shown in Fig. 7. The Mo- and S-rich limits correspond to those at 0 K, i.e., $\mu_S = -1.25$ eV and $\mu_S = 0$ eV, respectively. In addition to the neutral state, we found only one stable charge state: -1. The discontinuity in the formation energy graph describes the position of the $(0/-1)$

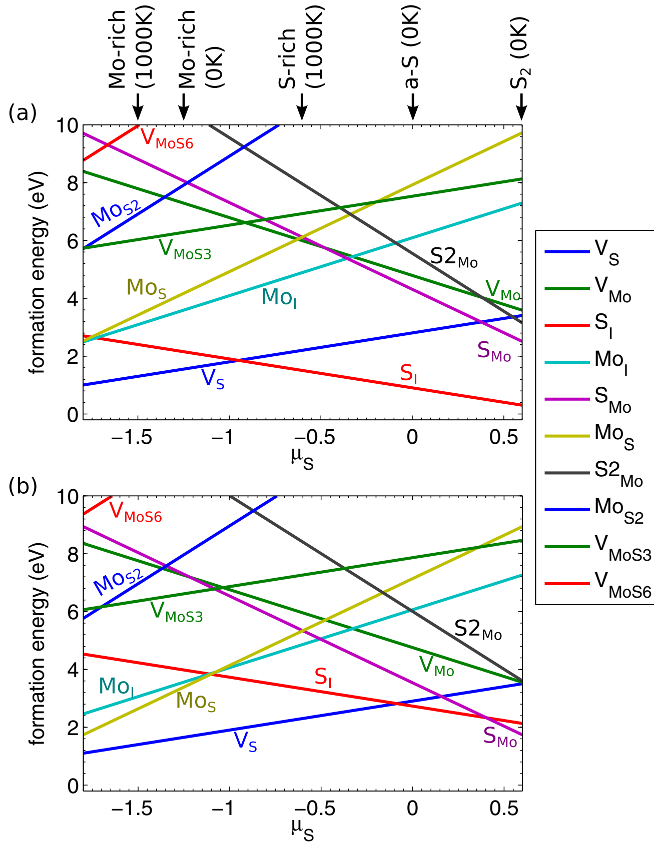

FIG. 6. (Color online) Formation energies of all considered defects in their neutral charge state as a function of the S chemical potential in (a) monolayer and (b) bulk. The Mo chemical potential is determined using the equilibrium condition [Eq. (6)] and $T = 0$ K.

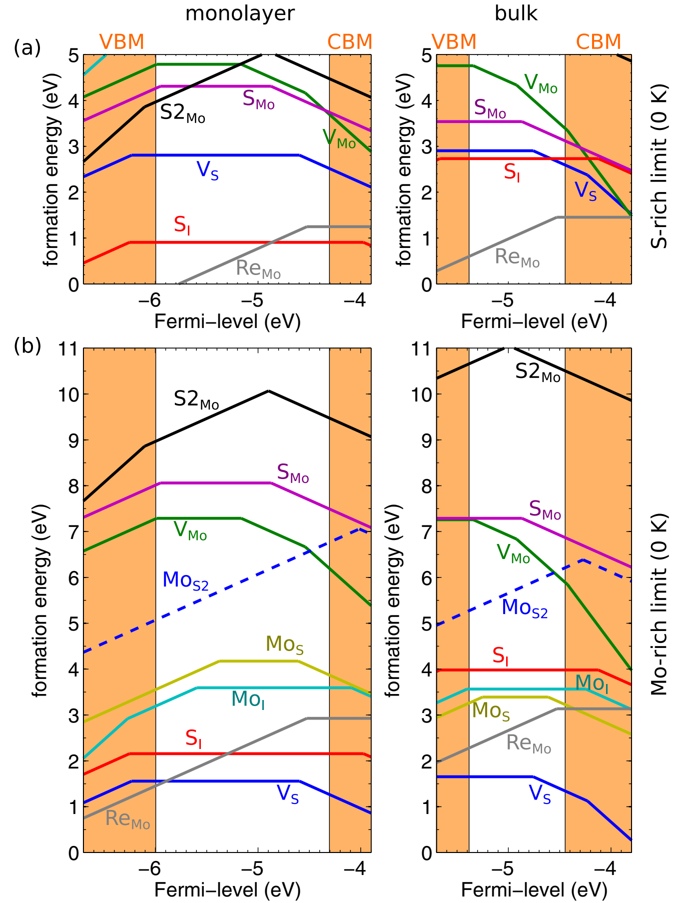

FIG. 7. (Color online) Formation energies as a function of the Fermi-level position calculated with the PBE-D functional for monolayer (left) and bulk (right) in the S-rich (top, $\mu_S = 0$ eV) and Mo-rich (bottom, $\mu_S = -1.25$ eV) chemical potentials, corresponding to 0 K. The coloring of the lines is the same as in Fig. 6. PBE-D calculated band edge positions are also shown. The energy zero of the Fermi level in both cases is at vacuum.

charge transition level. As this electron is added to the double degenerate defect state, the system undergoes a Jahn-Teller distortion and the symmetry is broken to C_s. In bulk, -2 becomes stable slightly above the CBM, with the parallel spin configuration ($m = 2\mu_B$) lower in energy by 45 meV. In monolayer, $+1$ becomes stable slightly below VBM. Taking into account the underestimation of band gap by PBE, these charge states might end up in the gap. Nevertheless, for all practical conditions, V_S is either in neutral or negative charge state and is thus always an acceptor.

B. Molybdenum vacancy and vacancy complexes

The geometry of the Mo vacancy, as shown in Fig. 5(b), does not undergo significant distortion from the pristine lattice, similar to S vacancy. Again, it behaves very similarly both in the monolayer and in the bulk. The threefold rotation symmetry is retained, yielding D_{3h} point group. As seen in Fig. 6, the formation energy of V_{Mo} is above 3 eV even in the extreme S-rich conditions, and thus their formation will be unlikely.

The electronic structure features five defect states in the gap occupied by four electrons and with zero magnetic moment [112,121]. From this it is clear that a large number of positive and negative charge states may be stable. As shown in Fig. 7, the stable charge states in monolayer are $+1$, 0, -1, and -2. In monolayer, since $+1$ is stable only in strongly p-type conditions, V_{Mo} behaves as an acceptor. In bulk, the charge states vary from 0 even up to -3. The neutral charge state is stable only at very p-type conditions, and thus V_{Mo} is a "strong" acceptor. In the case of two added electrons, the spin-paired configuration (no magnetic moment) is favored: 20 and 14 meV for monolayer and bulk, respectively.

We also considered two larger vacancy clusters consisting of both Mo and S vacancies, V_{MoS3} and V_{MoS6}, that were identified in the TEM studies of monolayer MoS_2 [39]. It is worth keeping in mind that electron beam is known to lead to S sputtering [38], which may have played a role in the formation of such large defects. The structures are shown in Figs. 5(c) and 5(d). The lone S atoms of V_{MoS3} are located out of the Mo plane and should be easily sputtered by the electron beam. In our calculation, V_{MoS3} was found to be nonmagnetic whereas V_{MoS6} has magnetic moment $6\mu_B$. Upon forming the V_{MoS3}, there is considerable binding between the Mo and S vacancies: $E_f(V_{MoS3}) - [E_f(V_{Mo}) + 3E_f(V_S)] = -5.65$ eV. For V_{MoS6}, there is no additional gain in energy and the formation energy difference is about the same. Nevertheless, being large defects,

the formation energies for both of these defects over the whole range of relevant chemical potentials is very high, as can be seen from Fig. 6.

C. Antisites

In the case of antisites, we have considered substitutions involving either one or two S atoms. For the former, there are the obvious candidates S_{Mo} and Mo_S. In addition, candidates where the substitution involves two S atoms (the S column), $S2_{Mo}$ and Mo_{S2}, were proposed on the basis of STEM imaging [39]. Moreover, they should play an important role in the dislocation and grain boundary structures [129]. Optimized geometries for all these are shown in Figs. 5(e)–5(h). Mo in Mo_{S2} and S2 in $S2_{Mo}$ are both displaced out of plane. Also, the S-S bond is broken in the case of $S2_{Mo}$.

On the basis of the calculated formation energies in Fig. 6, the single S antisites (S_{Mo} and Mo_S) are always found to be lower in energy than their S2 counterparts. S_{Mo} can have fairly low formation energy at high μ_S values, but will likely be of no concern at realistic growth conditions, as discussed later. The situation is rather similar for Mo_S at 0 K, but these defects will be more likely to form at high temperatures due to the lowering of chemical potential limits.

In the case of single S antisites, both $+1$ and -1 charge states are found to be stable with levels in the gap. Both of the S2 antisites are negative-U defects without stable neutral charge state. The $+1/-1$ level is located within the gap for $S2_{Mo}$, but it is pushed into the CBM for Mo_{S2}. Therefore, Mo_{S2} is always a donor in the $+1$ charge state.

D. Adatoms and interstitials

For adatoms on monolayer, we have considered three inequivalent positions, as illustrated in Fig. 8(a): (A) center of hexagon, (B) on top of the S atom, and (C) on top of the Mo atom. In the case of bulk, due to the particular stacking sequence of 2H-MoS_2, there exists only two inequivalent positions: (A) at the center of hexagon and (B) between the Mo and the S atoms of the surrounding layers. In addition, it was found in Ref. [112] that the lowest energy Mo interstitial is the split-interstitial configuration. This structure is shown in Fig. 5(i).

The only stable configuration for the S adatom on monolayer MoS_2 is on top of the S atom (B site) [Fig. 8(b)]. There are no partially filled states (only few occupied states very close to VBM) and therefore the only possible magnetic moment is zero. The formation energy in the S-rich limit is found to be very low. Being on top of the layer, however, they will readily interact with the environment during growth, processing, and characterization of the samples.

In bulk, the S interstitial was found to be stable at both inequivalent sites, but the center of hexagon (A site) is higher in energy by 1.17 eV. Thus, the formation energies for S interstitial correspond to the B-site configuration [Fig. 8(f)].

The case of a Mo adatom on a monolayer is slightly more complicated. Both A and C sites were found to be stable, with the relaxed geometries shown in Figs. 8(c) and 8(d). The C site, with Mo on top of Mo, is the more stable of the two by 0.26 eV. The partially filled 4d-derived states in the midgap enable formation of magnetic moment at the defect. We considered four cases where the magnetic moment was fixed to $0\mu_B$, $2\mu_B$, $4\mu_B$, or $6\mu_B$ during the calculation. For

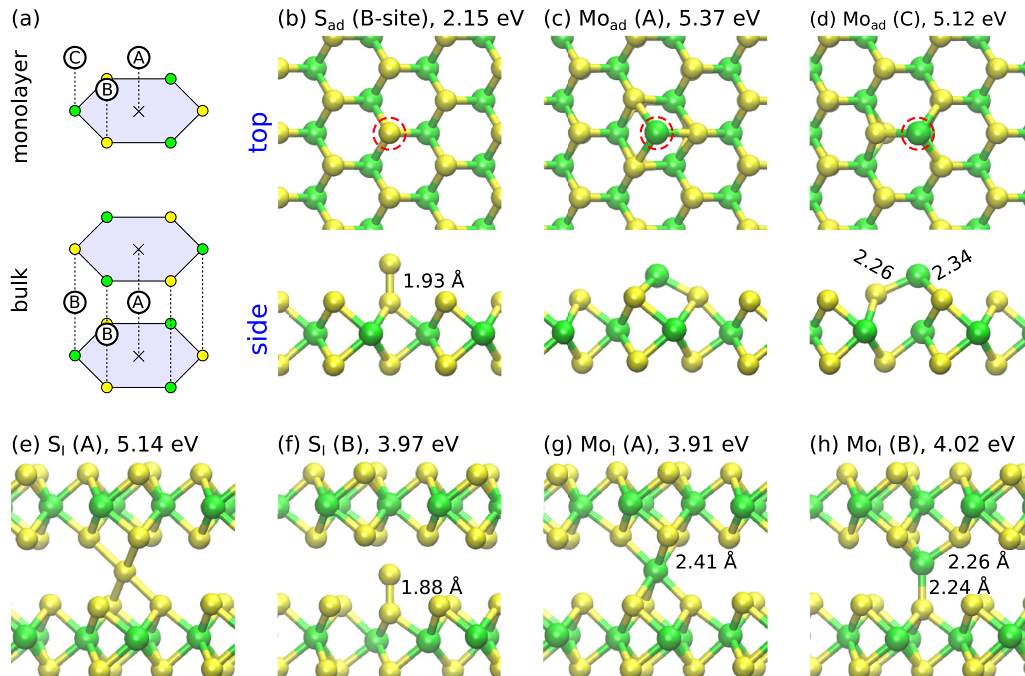

FIG. 8. (Color online) Final optimized geometries of the defects outside MoS_2 layer or between layers in the bulk: adatoms of monolayer MoS_2 (b)–(d) and interstitials in bulk MoS_2 (e)–(h). In the top views, a dashed (red) circle denotes the position of the adatom. The formation energies in the neutral charge state are also given along with selected bond lengths. (a) Schematic representation and labeling of the considered three inequivalent adatom sites on monolayer and corresponding two inequivalent interstitial sites in bulk.

both stable sites, $m = 4\mu_B$ is the lowest energy configuration, in agreement with Ref. [121].

However, the interstitial Mo can also form a split-interstitial configuration with the Mo in the pristine MoS_2 lattice [112]. The optimized geometry is shown in Fig. 5(i). The formation energy of $Mo_{I,split}$ is 1.51 eV lower than the C-site Mo_I. The magnetic moment is zero. In addition to the neutral state, we found only one other stable charge state, +1, with the corresponding level fairly close to the VBM.

Also, for Mo interstitial in bulk MoS_2 both inequivalent sites were found stable. The geometries are shown in Figs. 8(g) and 8(h). Unlike in the case of the Mo adatom, the A site (at the center of hexagon) now gives the lowest energy and with zero magnetic moment. For the B site the energies are very similar for magnetic moments of zero and two, residing 0.11–0.14 eV above the A-site configuration.

Quantitatively similar to the monolayer, the split interstitial configuration is again more stable than either the A or the B site. Qualitatively, however, the energy gain amounts to only 0.33 eV. In fact, since the +1/0 level of the B-site Mo_I is higher in the gap, its formation energy is slightly lower than for $Mo_{I,split}$ when Fermi energy is close to VBM. Still, for the sake of consistency between monolayer and bulk results, the energies for Mo_I in Figs. 6 and 7, and throughout the paper, correspond to the split-interstitial configuration.

E. Re impurity

Rhenium is a common impurity in natural MoS_2 samples [130]. They have also been introduced to synthetic samples [15,131,132] in order to produce *n*-type doping. Earlier computational studies confirmed the *n*-type (shallow donor) behavior [132,133]. The Re impurity prefers to be substituted into the Mo site, as evidenced by the atomic resolution transmission electron microscopy and computational studies in Ref. [132].

Being a shallow defect in the bulk phase, proper modeling of the defect wave function within the periodic supercell approach requires large supercell in order to avoid wave-function overlap and to accurately determine the ionization energy. Here we have used a 10×10 supercell for the monolayer and a $10 \times 10 \times 1$ supercell (i.e., two layers) for the bulk. The defect wave function is visualized in Fig. 9 showing slowly decaying tails and no significant directional dependence within the sheet, typical of a hydrogenic shallow defect. Note that only 62% of the charge density is contained within the isosurface depicted in the figure. It is important, however, that the wave function is almost completely localized (92%) within the layer in which the impurity resides. Consequently, the interaction and band dispersion in the direction perpendicular to the layers is minimal.

The formation energies shown in Fig. 7 show clearly why Re_{Mo} is an important defect in MoS_2. Even the neutral state formation energy is low and further decreases when moving to the *p*-type conditions.

In both cases, the charge transition level is very close to the conduction band edge, as expected from shallow donor. The ionization energies, when calculated using only the Kohn-Sham levels [134], are 50 meV for 2H-MoS_2 and 100 meV for the monolayer. The charge transition levels in Fig. 7 yield 80 meV for the bulk and 220 meV for the monolayer. These are in good agreement with the experimentally observed shallow donor level residing 50–90 meV below CBM [43,135]. In the monolayer case, the ionization energy is increased due to quantum confinement perpendicular to the layers, which may slightly undermine its efficiency for doping.

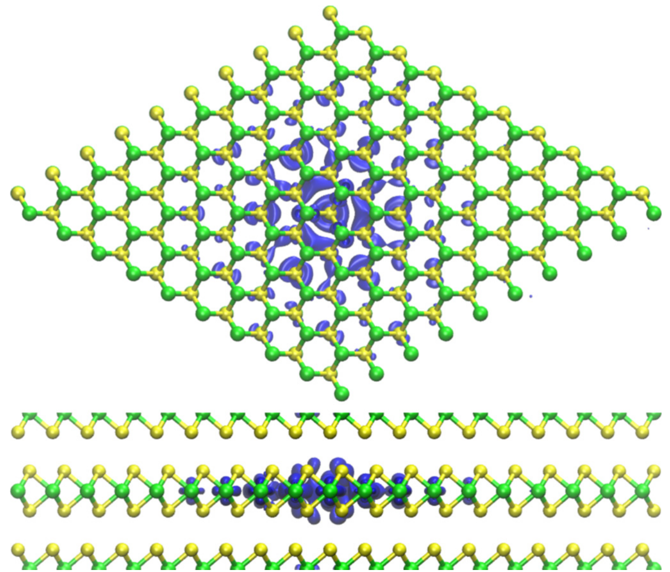

FIG. 9. (Color online) Top and side view of partial charge density isosurface from the wave function of the Re substitutional defect in the Mo site in 2H-MoS_2.

F. Charge transition levels

It is difficult to obtain reliable formation energies from the experiments. Some information about the defect concentrations, on the other hand, can be extracted and compared to the calculations. In addition, the charge transition levels can be extracted from the experiments, for instance, by probing carrier concentrations or capacitance as functions of external bias and temperature, or at the surface by using scanning tunneling spectroscopy (STS). Their assignment to any particular defect is still difficult without any modeling input.

When attempting to computationally determine the position of the defect levels inside the band gap, the underestimation of the gap with semilocal functionals such as PBE-D is obviously problematic. The situation can to some extent be remedied by using hybrid functionals to open up the gap. Here we adopt the HSE06 functional, which is known to work well for 3D semiconductor systems. It unfortunately fails to describe the van der Waals interactions, but this should not be a serious shortcoming for the defects within the layer.

The formation energies calculated with the two functionals for a few selected cases are shown in Fig. 10. The PBE-D and HSE results are very similar for V_S, but differ by about 1 eV for V_{Mo}. In 3D semiconductor systems, HSE has been reported to yield generally larger formation energies than PBE [75], in agreement with our findings. For adatoms and interstitials, HSE may also give larger formation energies due to the missing van der Waals binding. The discrepancy can partly also be due to the energy of the elemental phases. However, ΔH's

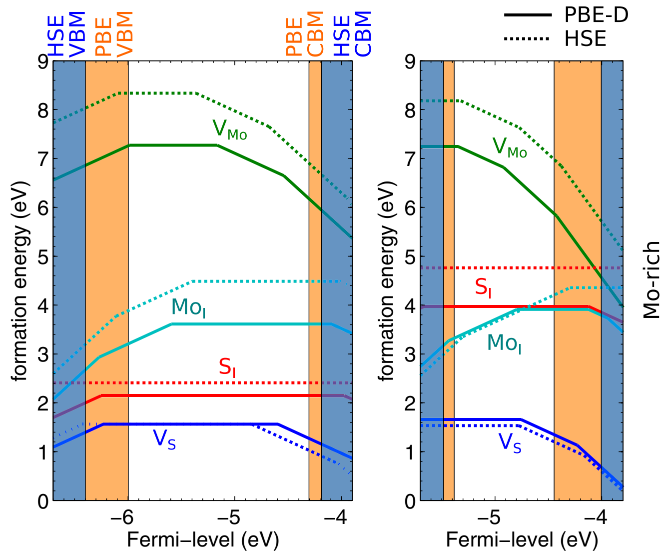

FIG. 10. (Color online) Comparison of PBE-D and HSE calculated formation energies at 0 K and Mo-rich limit for monolayer (left) and bulk (right) MoS_2.

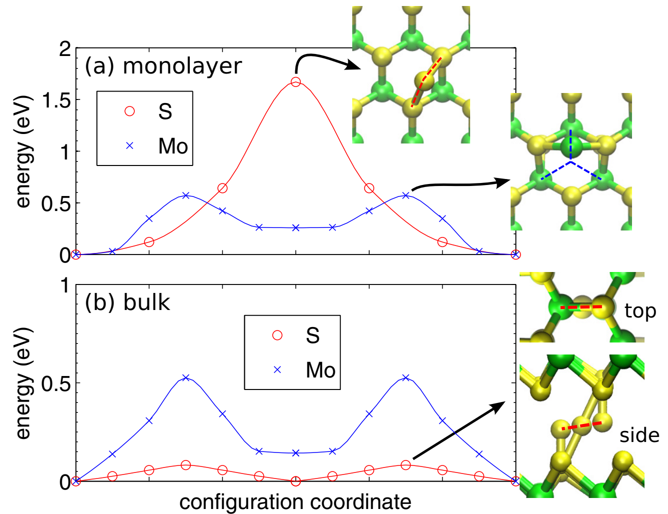

FIG. 12. (Color online) Energy along the migration path for diffusion of (a) adatoms on the monolayer surface and (b) interstitials inside bulk. Insets of (a) illustrate the saddle-point configurations for Mo and S migration paths on monolayer. Dashed lines illustrate the whole path. Insets of (b) show the saddle-point configuration and migration path for S interstitial. The path for Mo is similar to that in (a), but starting from the center of hexagon.

calculated with the two functionals are similar, and thus we expect the differences to indeed reflect different electronic description.

In contrast to the formation energies, the charge transition levels calculated with the two functionals agree well when given with respect to vacuum level, in accordance with the similar studies in bulk systems [73,113,114]. Furthermore, the defect levels in monolayer and bulk appear to be very close, in particular for the defects confined within the material sheet, as can be seen from Fig. 11.

The PBE-D calculated 0/−1 level of V_S, which is the most relevant for this study, is located 0.29 eV below CBM in monolayer and 0.31 eV below CBM in bulk. With the HSE functional, it is located 0.65 eV below CBM for monolayer and 0.77 eV below CBM for bulk. It is then curious that the two experimental reports give 0.27 eV below CBM [43], in agreement with PBE-D, and 0.7 eV below CBM [44], in agreement with HSE. Neither measurement can be unambiguously assigned to S vacancies, but the peak in the STS spectrum reported in Ref. [44] clearly originates from point defects on the surface or subsurface layers. We think that the HSE result might be closer to reality since HSE gives fundamental band gap and electron affinity in better agreement with the experiments.

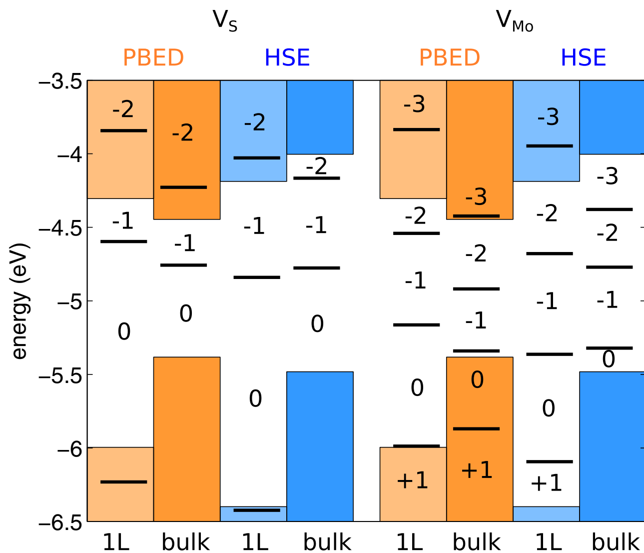

FIG. 11. (Color online) Comparison of the S and Mo vacancy charge transition level positions within the gap between monolayer and bulk and as calculated with the PBE-D and HSE functionals.

G. Diffusion of interstitials and adatoms

When considering growth dynamics, diffusion barriers can be as important as the formation energies. The migration barrier for S vacancy diffusion in monolayer MoS_2 was calculated at the PBE level to be 2.3 eV [127]. The barrier is expected to be of similar magnitude for the bulk, and thus the vacancy migration is insignificant at temperatures below 400° C, but may play a minor role at growth temperatures.

The migration barriers for adatoms on the surface of a monolayer and for interstitials in bulk are shown in Fig. 12 with illustrations of the migration paths. We first consider adatoms on monolayer. Since there is only one local minimum for S adatom, the diffusion has to proceed from one S site to another. As can be seen in Fig. 12, the migration barrier is fairly high, 1.67 eV. In the case of the Mo adatom, the diffusion can proceed more easily since there are two stable sites. The migration barrier from the lowest energy site on top of Mo to the site in the center of hexagon is 0.57 eV (at magnetic moment fixed to four). This is low enough to allow diffusion even at room temperature.

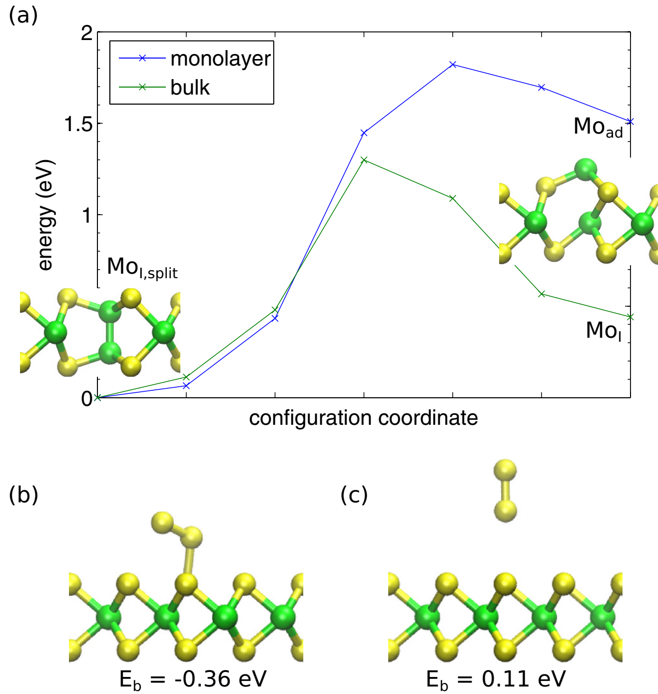

FIG. 13. (Color online) (a) Energy barrier for the Mo migration from the adatom or interstitial site to the $Mo_{I,split}$ configuration. The energy of $Mo_{I,split}$ is set to zero both in bulk and in monolayer. (b),(c) Visualization of the two (meta-)stable configurations for S_2 molecule on top of MoS_2 and the binding energy $E_b = E(MoS_2) + E(S_2) - E(MoS_2 + S_2)$ (a positive value corresponds to binding to the surface).

In the bulk, due to the two sites being equivalent, S diffusion can easily proceed via the neighboring Mo/S sites. We then find a dramatic drop in the migration barrier down to 0.08 eV, in contrast with the 1.67 eV at the surface. The migration path is illustrated in the insets of Fig. 12(b) and shows that the interstitial S atom remains almost exactly at the middle of the two layers. This is expected to yield extremely rapid diffusion even at low temperatures. Starting from the most stable center-of-hexagon site, Mo diffusion has to pass through the Mo/S site. The migration path is otherwise similar to that of adatom on the surface of monolayer. The migration barrier is determined between these two sites (with magnetic moment fixed to zero) and found to be 0.53 eV, similar to that found for Mo adatom diffusion on surface. We also considered the barrier for Mo migration from the Mo_{Ad} or Mo_I configuration to the $Mo_{I,split}$ one. The results are shown in Fig. 13(a). The barriers are 0.86 eV in bulk and only 0.31 eV in monolayer. Therefore, it should be fairly easy for a diffusing Mo adatom or interstitial to overcome the barrier and get locked into the split-interstitial configuration.

The results are collected in Table II. To sum up, at room temperature some Mo diffusion occurs both on the surface and between the layers, but can get locked into the split interstitial configuration. On the other hand, S atoms are relatively strongly bound to the surface, but are extremely mobile between the layers. At growth temperatures, all of these can occur to some extent. The extremely small diffusion barrier of S_I can be useful, for example, to heal the vacancies through sulfurization. Particularly in vertically aligned structures [11], S can intercalate through the edges and then migrate easily.

TABLE II. Migration barriers (in eV) for the diffusion of Mo and S interstitials in bulk and correspondingly in the cases of Mo and S adatoms on monolayer. In the case of Mo, we also report the barrier from interstitial/adatom site to the split-interstitial site. The result for S vacancy is taken from Ref. [127].

	$S_I \to S_I$	$Mo_I \to Mo_I$	$Mo_I \to Mo_{I,split}$	$V_S \to V_S$
Monolayer	1.67	0.57	0.31	2.3
Bulk	0.08	0.53	0.86	

Finally, due to the possibly large concentration of S adatoms on the surface, it is worth considering what would happen when two of these adatoms meet. We found that they will readily form S_2 molecules. Starting from two S_{Ad}'s in the nearest-neighbor sites and slightly displaced closer to each other, we obtained a metastable state shown in Fig. 13(b). The energy gain vs two S_{Ad}'s is -0.29 eV, but 0.36 eV higher than with completely desorbed S_2 molecule. However, another configuration where the S_2 is weakly physisorbed on top of the S site perpendicular to the layer, as shown in Fig. 13(c), yielded energy gain vs two S_{Ad}'s of -0.76 eV and was bound to the surface by 0.11 eV. Nevertheless, these results suggest that as two S adatoms meet, they form a S_2 molecule which will be very easily desorbed from the surface. Thus, although the S adatom formation energy is low, its concentration will be lowered by the S_2 formation and desorption process. This, in turn, can have implications for the growth kinetics. Low S concentration of the surface can lead to preferential growth from the edges and thus favor monolayer formation [30].

IV. THERMODYNAMIC CALCULATIONS

We now move on to calculating defect concentrations and Fermi-level position self-consistently at thermal equilibrium and under different chemical conditions. In particular, we focus on the conditions that are relevant to (CVD) grown samples of bulk MoS_2. The calculation procedure is described in Appendix A . The temperature dependence of the chemical potentials were described in the Methods section. The formation energy changes through the chemical potentials but also through the free energies in Eq. (2). For S vacancy, we have explicitly calculated the free energy as a function of temperature using the quasiharmonic approximation as described in Appendix B . Since the effect of T to the formation energy is only 0.1–0.2 eV, we have not performed these calculations to other higher formation energy defects. Ideally, we should also take into account the temperature effect on the band gap (and on the lattice constant). The PBE band gap of 0.95 eV is roughly 0.35 eV smaller than the experimental gap at 0 K. However, knowing that the band gap decreases by about 0.4 meV/K [136,137], we estimate that experimentally a band gap of 0.95 eV would be obtained at 875 K (600° C), which is close to the growth temperatures. In fact, the same is true for lattice constants. PBE overestimates the lattice constant by about 0.02 Å, which corresponds to thermal expansion of the lattice at 600 °C [138–140]. That is, for the band gap and lattice constants at high temperature, PBE-D values are in

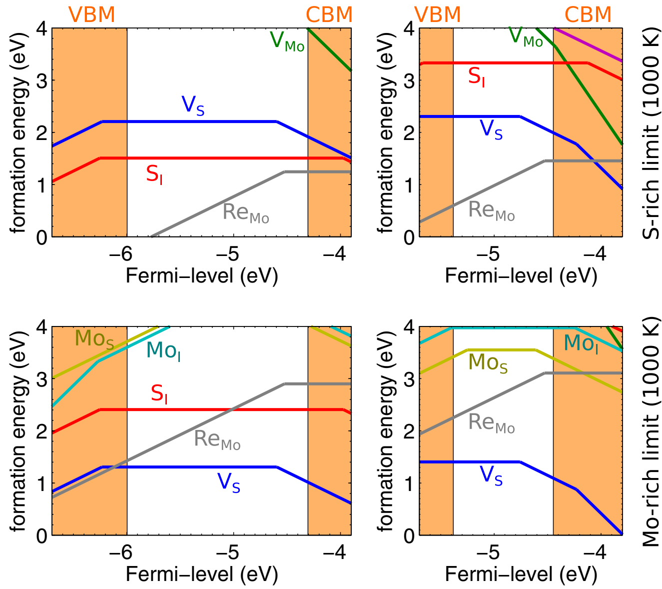

FIG. 14. (Color online) Formation energies at 1000 K as a function of the Fermi-level position for monolayer (left) and bulk (right) in the S-rich (top, $\mu_S = -0.6$ eV) and Mo-rich (bottom, $\mu_S = -1.5$ eV) chemical potentials. The coloring of the lines is the same as in Fig. 6. PBE-D calculated band edge positions are also shown. The energy zero of Fermi level in both cases is at vacuum.

much better agreement with experiment than the HSE ones, and thus we have adopted PBE-D in the following.

In Fig. 14 we show the formation energies pertaining to 1000 K temperature in Mo- and S-rich ($p = p^0$) limits, properly accounting for the temperature dependence of the chemical potentials. Compared to the 0 K values in Fig. 7, V_{Mo} or S_I have moved to higher energy. Even more clearly than before, the only defects that need to be considered are V_S, S_I, and Re_{Mo}. The prefactors needed in Eq. (1) for these defects are $N_0 = N_{MoS2}$ and N_c equals to 2 for V_S, and 1 for V_{Mo} and Re_{Mo}. For interstitials, $N_c = 1$ and 2 for the center of hexagon and Mo-S sites, respectively.

A. Equilibrium defect concentration

There are very little experimental data about the equilibrium defect concentrations in bulk MoS_2, native or synthetic, which already suggests that the defect concentrations are likely to be small. Indeed, in Ref. [40], the number of defects on the surface of natural cleaved molybdenite was counted to be 10^7 cm^{-2}(10^{-6}% of the primitive cells at the surface contain defect) and assumed to be vacancies. Furthermore, the concentration seemed to be largely independent of the source of the natural sample. However, the used method was very indirect. On the other hand, very high S vacancy concentration of 10^{13} cm^{-2} ($\sim$1%). was reported in [32], but after vacancy annealing, which has been suggested to lead to production of additional S vacancies [37,58]. In addition, in relation to the presumably vacancy-derived CBM-0.27-eV defect level (cf. Sec. III F), a concentration of 3.2×10^{11} cm^{-2} ($\sim$0.03%) was reported [43], and in relation to the CBM-0.7-eV defect level, a concentration of 3.5×10^{10} cm^{-2}($\sim$0.003%) [44].

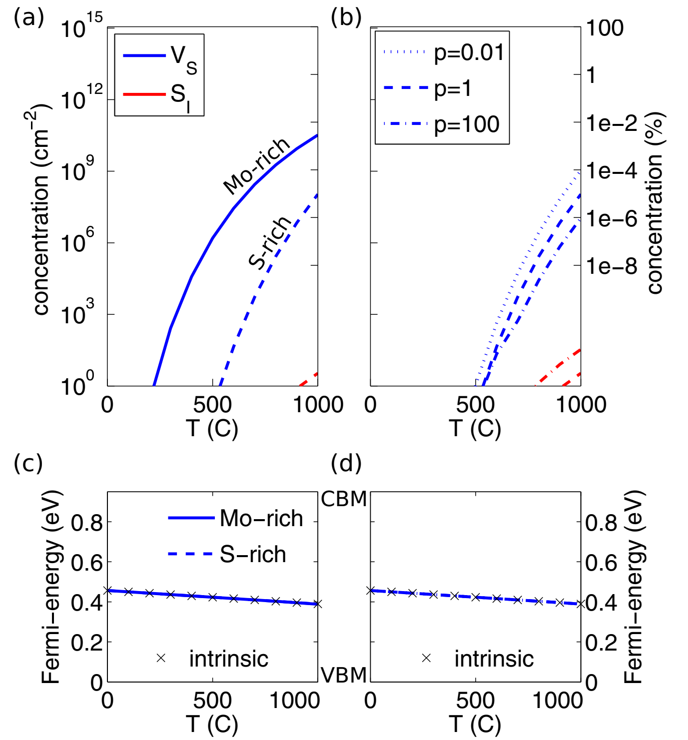

FIG. 15. (Color online) (a),(b) Defect concentrations in bulk MoS_2 as a function of temperature for (a) Mo- and S-rich limits ($p = 1$ bar) and (b) S-rich limit with $p = 0.01$ bar, $p = 1$ bar, and $p = 100$ bar. (c),(d) The respective Fermi-level positions within the band gap. Crosses denote positions of the intrinsic Fermi level.

The results from our calculations for systems without rhenium are shown in Fig. 15. In Fig. 15(a) is shown the equilibrium defect concentrations as a function of temperature in both the Mo-rich and the S-rich (with $p = 1$ bar) limits. It is immediately clear that over the whole range of chemical potentials significant defect concentrations are obtained only for the S vacancy. Figure 15(b) shows the results at the S-rich limit as S partial pressure changes from 0.01 to 100 bar. Within this pressure range, the concentration of S vacancies at 1000 K changes by about two orders of magnitude, but is still below the values from the Mo-rich limit. On the other hand, high-quality crystal with a small number of defects should be obtainable by increasing the S pressure.

The evolution of the Fermi-level position in the system is also shown in Fig. 15. In all considered growth conditions, the Fermi level is indistinguishable from the intrinsic Fermi-level position,

$$E_{F,i} = \frac{E_g}{2} + \frac{k_B T}{2} \ln \frac{N_v}{N_c}, \quad (9)$$

where N_v and N_c are the valence and conduction band effective density of states, respectively. Not only is the S-vacancy concentration very low, but, being a deep acceptor, the defect remains mostly in the neutral charge state and thus does not contribute to the Fermi-level position.

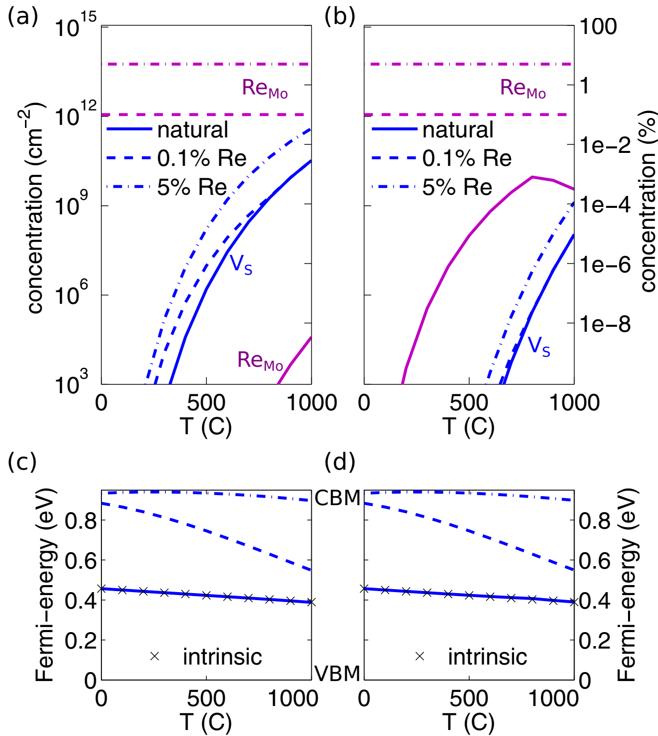

FIG. 16. (Color online) (a),(b) Defect concentrations as a function of temperature including Re doping in (a) Mo-rich and (b) S-rich ($p = 1$ bar) conditions. Three different doping levels are shown: intrinsic, 0.1%, and 5%. (c),(d) The respective Fermi-level positions within the band gap.

B. Re-doped 2H-MoS_2

Next, Re impurities are introduced to the system. Re is present in many natural samples, but can also be used as an external impurity in CVD grown samples to yield n-type doping. We consider cases where either some particular Re concentration is fixed during the growth or the intrinsic Re concentration at equilibrium is determined using the same procedure as for all other defects. The typical Re concentrations in natural samples fall around 0.001%–0.2% [130]. The maximum Re concentration we consider is 5%, since MoS_2 and ReS_2 are immiscible at more than 5% Re [15].

The defect concentrations are shown in Fig. 16. In Mo-rich conditions, the Re concentration remains very low. However, in the S-rich conditions, the Re concentration approaches 10^{10} cm^2 or 0.001%, which is in the lower side of the experimentally observed concentrations. The kink at 800° C is a result of the change in the chemical potential reference, as bulk Re becomes more stable than the equilibrium with ReS_2.

High Re concentrations shift the Fermi level close to the conduction band minimum. This, in turn, means that the formation energy of S vacancy decreases as the -1 charge state starts to dominate. Consequently, the S vacancy concentration is higher than in the undoped samples. On the other hand, increasing number of V_S in the -1 charge state contributes to the Fermi-level shifting back to the middle of the band gap. Therefore, whenever the final sample is n-type doped, then the vacancy concentration should also be high. On the other hand, higher Re concentrations could be promoted by moving the Fermi level closer to the valence band, i.e., by p-type doping.

C. Discussion

The concentration of S vacancies at high temperatures can be at most 10^8 cm^{-2} in the S-rich limit, 10^{10} cm^{-2} in the Mo-rich limit without Re, and 10^{11} cm^{-2} in the Mo-rich limit with large concentration of Re. These values are in reasonable agreement with the 10^7 cm^{-2} surface vacancy concentration reported by Bahl *et al.* [40]. The 10^{10}–10^{11} cm^{-2} observed in exfoliated monolayer samples [43,44] are within the limits calculated here, although there may have been additional sources for vacancies such as extrinsic n-type dopants, growth kinetics, or device processing steps.

In agreement with experiments, we find S vacancies to be the most abundant native defects in all relevant conditions, but being deep acceptors they cannot be the cause of the n-type doping. Consequently, native defects in general are unlikely to be the cause of the n-type doping, which should then be assigned to other impurities (such as Re) or in the case of monolayer possibly to interaction with the environment.

The reason that we have concentrated mostly on the growth of bulk MoS_2 is due to the multitude of additional issues in the growth of monolayer materials. All molecules that are present during the growth also interact with the substrate. Not only can it affect the kinetics of the growth, but also the defect formation energies. It is also important to realize that the substrate can determine the Fermi level which, in turn, can affect the concentrations. For example, the SiO_2 substrate appeared to yield negative charging of MoS_2 [61]. In addition, any molecules on the surface of the grown layer can also affect the Fermi level and defect formation energies.

V. CONCLUSIONS

We have calculated formation energies and thermodynamical charge transition levels for a large set of neutral and charged native defects in bulk and monolayer MoS_2. With all this information in hand, we applied a self-consistent scheme to determine thermal equilibrium defect concentrations and Fermi-level position in the system as a function of temperature and of the chemical potentials. We also studied the diffusion of adatoms and interstitials in these systems, as well as the role of Re doping, a common extrinsic impurity.

We show that the effect of temperature and growth conditions on all relevant computational quantities such as the formation energies and chemical potentials have to be carefully accounted for. To this end, we have given a detailed description of the computational methodology needed to carry out these calculations. By studying the bulk and monolayer on an equal footing, we can shed light on the transferability of results between these phases.

We summarize our findings as follows. (1) Both S and Mo vacancies are always acceptors and thus cannot be the cause of n-type doping, whereas adatoms and interstitials can have different behaviors; (2) S vacancies are the most abundant defects at all practical growth conditions, but especially so in the Mo-rich conditions. (3) Under S-rich conditions, all formation energies are relatively high and good-quality crystal

growth is expected. (4) Re doping pushes the Fermi level close to the conduction band, which further favors formation of both S (and Mo) vacancies. (5) Migration barrier of the S interstitial in bulk is extremely low and rapid diffusion is expected. (6) S adatoms on the surface are bound to the surface fairly strongly, but as two adatoms meet the resulting S_2 molecule is easily desorbed. (7) Formation energies and charge transition levels for vacancies in bulk and in monolayer are similar.

The calculated results provided here for the native defects in MoS_2 are expected to be useful for understanding and optimizing the growth conditions, but also to pave the way for further work to examine the role of other elements that may be present during the growth. Moreover, we hope that the presented methodology encourages further studies on defects in 2D materials where the role of thermodynamic parameters is properly accounted for, and eventually leads to computational predictions in qualitative and even quantitative agreement with the experiments.

ACKNOWLEDGMENTS

The work was carried out with partial financial support from the Academy of Finland through Project No. 263416. H.P.K. further thanks the Academy of Finland for the support through its Centres of Excellence Programme (2012–2017) under Project No. 251748. We also thank CSC-IT Center for Science Ltd. and Aalto Science-IT project for generous grants of computer time.

APPENDIX A: DEFECT CONCENTRATION CALCULATIONS

Our approach is similar to those described in, e.g., Refs. [92,141]. The system has to fulfill the charge neutrality condition,

$$p - n + \sum_{X,q} q c(X^q) = 0, \tag{A1}$$

where n and p are the concentrations of free electrons and holes. $c(X^q)$ are the concentration of defects in charge state q, where X runs over all defects and q over all stable charge states of X. The concentrations c are determined from the formation energy using Eq. (1). Care needs to be taken in finding the charge state distribution. We calculate the formation energies for all charge states using Eq. (2), determine the concentrations c' using Eq. (1), and normalize these concentrations over the charge states,

$$c(X^q) = c'(X^q)\frac{\max c'(X^q)}{\sum_q c'(X^q)}, \tag{A2}$$

where the maximum is taken over different charge states q. This way, the total concentration of defect X is always equal to the lowest formation energy, but the division among different charge states follows the formation energy differences. In particular, when E_F coincides with some charge transition level, the total defect concentration is divided equally between the two contributing charge states.

The free electron and hole concentrations are calculated using Fermi-Dirac distribution. To get the electron and hole concentrations, the density of states $D(E)$ is multiplied by the occupancy from Fermi-Dirac statistics $F(E)$ and integrated over the energy,

$$n = \int_{E_c}^{\infty} D(E)F(E)dE, \tag{A3}$$

where

$$F(E) = \frac{1}{1 + \exp[(E - E_F)/kT]}, \tag{A4}$$

and similarly for p. We carry out this integration numerically.

For the density of the states, we assume a parabolic dispersion relation of the form $E = E_0 + \frac{\hbar^2}{2m^*}k^2$, with m^* being the effective mass of the valley. The density of states, accounting for the spin quantum number in 3D is

$$D(E) = \frac{M}{2\pi^2}\left(\frac{2m^*}{\hbar^2}\right)^{3/2} E^{1/2} \tag{A5}$$

where M is the valley multiplicity: 1, 6, and 2 for the Γ, T, and K, respectively.

TABLE III. Effective masses at the band edges of bulk MoS_2 calculated using PBE-D.

	VBM		CBM	
	Γ	K	T	K
$m_{\parallel}$	0.7	0.58	0.66	0.50
$m_{\perp}$	0.95	2.4	0.67	100

The effective masses used in this work are obtained by fitting to the band structures and listed in Table III. The obtained effective masses are similar to those reported previously [142,143], but recalculated here for the sake of consistency.

All charge densities in Eq. (A1) depend on the Fermi-level position. It is then straightforward to find E_F that satisfies the equation and use that E_F to calculate all defect concentrations and charge states.

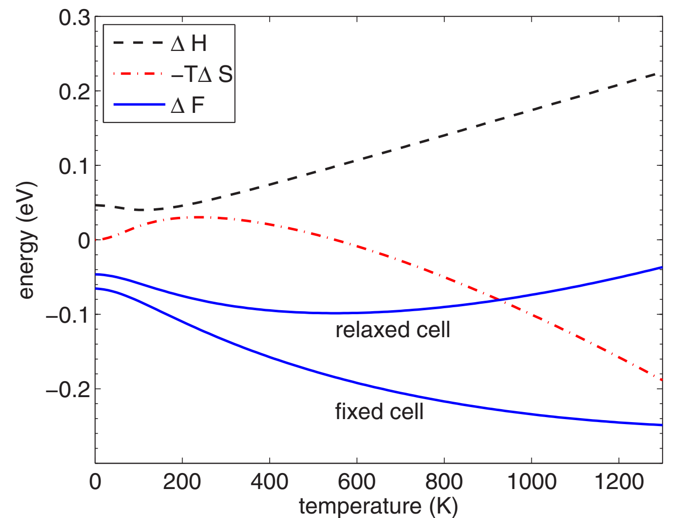

FIG. 17. (Color online) The change of free energy ΔF (solid blue line) and enthalpy ΔH (dashed black line) and entropy ΔS (dash-dotted red line) contributions to it, as a function of temperature for S vacancy in monolayer MoS_2.

APPENDIX B: DEFECT FREE ENERGY OF FORMATION

We evaluate the magnitude of the lattice vibrations on the defect formation energy as discussed in the Methods section and, in particular, the F^{qh} term in Eq. (3). We have neglected the anharmonic contributions, which may lead to errors in the range of 0.1–0.2 eV for the temperatures considered in this work, since the full treatment is computationally extremely demanding [144]. The vibrational properties and the thermochemical quantities are calculated using PHON program [102]. The calculation was carried out for the V_S defect in monolayer MoS_2 employing the 6×6 supercell.

The results are shown in Fig. 17. The free energy difference corresponds to $\Delta F = F(\text{vac}) - 36F(\text{MoS}_2)$ and similarly for the enthalpy and entropy terms. The free energy changes for the missing S are included in the chemical potentials in Eq. (2) and are thus not included in ΔF. We show the results for cases where the computational cell for the vacancy supercell has been allowed to relax or where it is fixed to the bulk cell. As the enthalpy and entropy contributions are of opposite sign, they largely cancel out and the total free energy changes only within 0.1 or 0.25 eV, depending on the cell relaxation. For the results given in Sec. IV we have used the values where cell parameters are relaxed.

[1] Q. H. Wang, K. Kalantar-Zadeh, A. Kis, J. N. Coleman, and M. S. Strano, Nat. Nanotechnol. **7**, 699 (2012).
[2] M. Chhowalla, H. S. Shin, G. Eda, L.-J. Li, K. P. Loh, and H. Zhang, Nat. Chem. **5**, 263 (2013).
[3] K. F. Mak, C. Lee, J. Hone, J. Shan, and T. F. Heinz, Phys. Rev. Lett. **105**, 136805 (2010).
[4] D. Xiao, G.-B. Liu, W. Feng, X. Xu, and W. Yao, Phys. Rev. Lett. **108**, 196802 (2012).
[5] K. F. Mak, K. He, C. Lee, G. H. Lee, J. Hone, T. F. Heinz, and J. Shan, Nat. Mater. **12**, 207 (2013).
[6] B. Radisavljevic, A. Radenovic, J. Brivio, V. Giacometti, and A. Kis, Nat. Nanotech. **6**, 147 (2011).
[7] S. Bertolazzi, J. Brivio, and A. Kis, ACS Nano **5**, 9703 (2011).
[8] A. Castellanos-Gomez, M. Poot, G. A. Steele, H. S. J. van der Zant, N. Agraït, and G. Rubio-Bollinger, Adv. Mat. **24**, 772 (2012).
[9] O. Lopez-Sanchez, D. Lembke, M. Kayci, A. Radenovic, and A. Kis, Nat. Nanotechnol. **8**, 497 (2013).
[10] D. Voiry, H. Yamaguchi, J. Li, R. Silva, D. C. B. Alves, T. Fujita, M. Chen, T. Asefa, V. B. Shenoy, G. Eda, and M. Chhowalla, Nat. Mater. **12**, 850 (2013).
[11] D. Kong, H. Wang, J. J. Cha, M. Pasta, K. J. Koski, J. Yao, and Y. Cui, Nano Lett. **13**, 1341 (2013).
[12] H. Li, Z. Yin, Q. He, H. Li, X. Huang, G. Lu, D. W. H. Fam, A. I. Y. Tok, Q. Zhang, and H. Zhang, Small **8**, 63 (2012).
[13] R. E. Bell and R. E. Herfert, J. Am. Chem. Soc. **79**, 3351 (1957).
[14] J. Wilson and A. Yoffe, Adv. Phys. **18**, 193 (1969).
[15] K. Tiong, Y. Huang, and C. Ho, J. Alloys Compd. **317-318**, 208 (2001).
[16] R. Tenne, L. Margulis, M. Genut, and G. Hodes, Nature (London) **360**, 444 (1992).
[17] Y. Feldman, E. Wasserman, D. J. Srolovitz, and R. Tenne, Science **267**, 222 (1995).
[18] R. Rosentsveig, A. Margolin, A. Gorodnev, R. Popovitz-Biro, Y. Feldman, L. Rapoport, Y. Novema, G. Naveh, and R. Tenne, J. Mater. Chem. **19**, 4368 (2009).
[19] S. Helveg, J. V. Lauritsen, E. Lægsgaard, I. Stensgaard, J. K. Nørskov, B. S. Clausen, H. Topsøe, and F. Besenbacher, Phys. Rev. Lett. **84**, 951 (2000).
[20] J. Kibsgaard, J. V. Lauritsen, E. Lægsgaard, B. S. Clausen, H. Topsøe, and F. Besenbacher, J. Am. Chem. Soc. **128**, 13950 (2006).
[21] Y. Zhan, Z. Liu, S. Najmaei, P. M. Ajayan, and J. Lou, Small **8**, 966 (2012).
[22] I. Song, C. Park, M. Hong, J. Baik, H.-J. Shin, and H. C. Choi, Angew. Chem., Int. Ed. **53**, 1266 (2014).
[23] Y.-H. Lee, X.-Q. Zhang, W. Zhang, M.-T. Chang, C.-T. Lin, K.-D. Chang, Y.-C. Yu, J. T.-W. Wang, C.-S. Chang, L.-J. Li, and T.-W. Lin, Adv. Mater. **24**, 2320 (2012).
[24] S. Najmaei, Z. Liu, W. Zhou, X. Zou, G. Shi, S. Lei, B. I. Yakobson, J.-C. Idrobo, P. M. Ajayan, and J. Lou, Nat. Mater. **12**, 754 (2013).
[25] A. M. van der Zande, P. Y. Huang, D. A. Chenet, T. C. Berkelbach, Y. You, G.-H. Lee, T. F. Heinz, D. R. Reichman, D. A. Muller, and J. C. Hone, Nat. Mater. **12**, 554 (2013).
[26] D. Kim, D. Sun, W. Lu, Z. Cheng, Y. Zhu, D. Le, T. S. Rahman, and L. Bartels, Langmuir **27**, 11650 (2011).
[27] K.-K. Liu, W. Zhang, Y.-H. Lee, Y.-C. Lin, M.-T. Chang, C.-Y. Su, C.-S. Chang, H. Li, Y. Shi, H. Zhang, C.-S. Lai, and L.-J. Li, Nano Lett. **12**, 1538 (2012).
[28] Y. Shi, W. Zhou, A.-Y. Lu, W. Fang, Y.-H. Lee, A. L. Hsu, S. M. Kim, K. K. Kim, H. Y. Yang, L.-J. Li, J.-C. Idrobo, and J. Kong, Nano Lett. **12**, 2784 (2012).
[29] R. Bichsel and F. Levy, J. Phys. D **19**, 1809 (1986).
[30] M. J. Cuddy, K. P. Arkill, Z. W. Wang, H.-P. Komsa, A. V. Krasheninnikov, and R. E. Palmer, Nanoscale **6**, 12463 (2014).
[31] D. Jena and A. Konar, Phys. Rev. Lett. **98**, 136805 (2007).
[32] H. Qiu, T. Xu, Z. Wang, W. Ren, H. Nan, Z. Ni, Q. Chen, S. Yuan, F. Miao, F. Song, G. Long, Y. Shi, L. Sun, J. Wang, and X. Wang, Nat. Commun. **4**, 2642 (2013).
[33] M. Ghorbani-Asl, A. N. Enyashin, A. Kuc, G. Seifert, and T. Heine, Phys. Rev. B **88**, 245440 (2013).
[34] S. McDonnell, R. Addou, C. Buie, R. M. Wallace, and C. L. Hinkle, ACS Nano **8**, 2880 (2014).
[35] S. W. Han, Y. H. Hwang, S.-H. Kim, W. S. Yun, J. D. Lee, M. G. Park, S. Ryu, J. S. Park, D.-H. Yoo, S.-P. Yoon, S. C. Hong, K. S. Kim, and Y. S. Park, Phys. Rev. Lett. **110**, 247201 (2013).
[36] T. Korn, S. Heydrich, M. Hirmer, J. Schmutzler, and C. Schüller, Appl. Phys. Lett. **99**, 102109 (2011).
[37] S. Tongay, J. Suh, C. Ataca, W. Fan, A. Luce, J. S. Kang, J. Liu, C. Ko, R. Raghunathanan, J. Zhou, F. Ogletree, J. Li, J. C. Grossman, and J. Wu, Sci. Rep. **3**, 2657 (2013).
[38] H.-P. Komsa, J. Kotakoski, S. Kurasch, O. Lehtinen, U. Kaiser, and A. V. Krasheninnikov, Phys. Rev. Lett. **109**, 035503 (2012).

[39] W. Zhou, X. Zou, S. Najmaei, Z. Liu, Y. Shi, J. Kong, J. Lou, P. M. Ajayan, B. I. Yakobson, and J.-C. Idrobo, Nano Lett. **13**, 2615 (2013).

[40] O. P. Bahl, E. L. Evans, and J. M. Thomas, Proc. R. Soc. London, Ser. A **306**, 53 (1968).

[41] G. Algara-Siller, S. Kurasch, M. Sedighi, L. Ossi, and U. Kaiser, Appl. Phys. Lett. **103**, 203107 (2013).

[42] R. Zan, Q. M. Ramasse, R. Jalil, T. Georgiou, U. Bangert, and K. S. Novoselov, ACS Nano **7**, 10167 (2013).

[43] J. Y. Kwak, J. Hwang, B. Calderon, H. Alsalman, N. Munoz, B. Schutter, and M. G. Spencer, Nano Lett. **14**, 4511 (2014).

[44] C.-P. Lu, G. Li, J. Mao, L.-M. Wang, and E. Y. Andrei, Nano Lett. **14**, 4628 (2014).

[45] M. José-Yacamán, H. López, P. Santiago, D. H. Galván, I. L. Garzón, and A. Reyes, Appl. Phys. Lett. **69**, 1065 (1996).

[46] C. B. Roxlo, H. W. Deckman, J. Gland, S. D. Cameron, and R. R. Chianelli, Science **235**, 1629 (1987).

[47] M. Baker, R. Gilmore, C. Lenardi, and W. Gissler, Appl. Surf. Sci. **150**, 255 (1999).

[48] J. B. Park, C. B. France, and B. A. Parkinson, J. Vac. Sci. Technol., B: Microelectron. Process. Phenom. **23**, 1532 (2005).

[49] S. Mathew, K. Gopinadhan, T. K. Chan, X. J. Yu, D. Zhan, L. Cao, A. Rusydi, M. B. H. Breese, S. Dhar, Z. X. Shen, T. Venkatesan, and J. T. L. Thong, Appl. Phys. Lett. **101**, 102103 (2012).

[50] A. Inoue, T. Komori, and K. ichi Shudo, J. Electron Spectrosc. Relat. Phenom. **189**, 11 (2013).

[51] O. Ochedowski, K. Marinov, G. Wilbs, G. Keller, N. Scheuschner, D. Severin, M. Bender, J. Maultzsch, F. J. Tegude, and M. Schleberger, J. Appl. Phys. **113**, 214306 (2013).

[52] T.-Y. Kim, K. Cho, W. Park, J. Park, Y. Song, S. Hong, W.-K. Hong, and T. Lee, ACS Nano **8**, 2774 (2014).

[53] Q. Ma, M. Isarraraz, C. S. Wang, E. Preciado, V. Klee, S. Bobek, K. Yamaguchi, E. Li, P. M. Odenthal, A. Nguyen, D. Barroso, D. Sun, G. von Son Palacio, M. Gomez, A. Nguyen, D. Le, G. Pawin, J. Mann, T. F. Heinz, T. S. Rahman, and L. Bartels, ACS Nano **8**, 4672 (2014).

[54] M. Chen, H. Nam, S. Wi, L. Ji, X. Ren, L. Bian, S. Lu, and X. Liang, Appl. Phys. Lett. **103**, 142110 (2013).

[55] S. Hosoki, S. Hosaka, and T. Hasegawa, Appl. Surf. Sci. **60-61**, 643 (1992).

[56] S. Hosaka, S. Hosoki, T. Hasegawa, H. Koyanagi, T. Shintani, and M. Miyamoto, J. Vac. Sci. Technol., B: Microelectron. Process. Phenom. **13**, 2813 (1995).

[57] B. W. H. Baugher, H. O. H. Churchill, Y. Yang, and P. Jarillo-Herrero, Nano Lett. **13**, 4212 (2013).

[58] M. Donarelli, F. Bisti, F. Perrozzi, and L. Ottaviano, Chem. Phys. Lett. **588**, 198 (2013).

[59] H. Qiu, L. Pan, Z. Yao, J. Li, Y. Shi, and X. Wang, Appl. Phys. Lett. **100**, 123104 (2012).

[60] K. Dolui, I. Rungger, C. Das Pemmaraju, and S. Sanvito, Phys. Rev. B **88**, 075420 (2013).

[61] D. Sercombe, S. Schwarz, O. D. Pozo-Zamudio, F. Liu, B. J. Robinson, E. A. Chekhovich, I. I. Tartakovskii, O. Kolosov, and A. I. Tartakovskii, Sci. Rep. **3**, 3489 (2013).

[62] J. Mann, D. Sun, Q. Ma, J.-R. Chen, E. Preciado, T. Ohta, B. Diaconescu, K. Yamaguchi, T. Tran, M. Wurch, K. Magnone, T. F. Heinz, G. L. Kellogg, R. Kawakami, and L. Bartels, Eur. Phys. J. B **86**, 226 (2013).

[63] M. M. Ugeda, A. J. Bradley, S.-F. Shi, F. H. da Jornada, Y. Zhang, D. Y. Qiu, W. Ruan, S.-K. Mo, Z. Hussain, Z.-X. Shen, F. Wang, S. G. Louie, and M. F. Crommie, Nat. Mater. **13**, 1091 (2014).

[64] G. Kresse and J. Hafner, Phys. Rev. B **47**, 558 (1993).

[65] G. Kresse and J. Furthmüller, Comput. Mater. Sci. **6**, 15 (1996).

[66] J. P. Perdew, K. Burke, and M. Ernzerhof, Phys. Rev. Lett. **77**, 3865 (1996).

[67] S. Grimme, J. Comput. Chem. **27**, 1787 (2006).

[68] T. Björkman, A. Gulans, A. V. Krasheninnikov, and R. M. Nieminen, Phys. Rev. Lett. **108**, 235502 (2012).

[69] T. Björkman, A. Gulans, A. V. Krasheninnikov, and R. M. Nieminen, J. Phys.: Condens. Matter **24**, 424218 (2012).

[70] J. Heyd, G. E. Scuseria, and M. Ernzerhof, J. Chem. Phys. **118**, 8207 (2003).

[71] J. Heyd, G. E. Scuseria, and M. Ernzerhof, J. Chem. Phys. **124**, 219906 (2006).

[72] P. Deák, B. Aradi, T. Frauenheim, E. Janzén, and A. Gali, Phys. Rev. B **81**, 153203 (2010).

[73] H.-P. Komsa and A. Pasquarello, Phys. Rev. B **84**, 075207 (2011).

[74] W. Chen and A. Pasquarello, Phys. Rev. B **88**, 115104 (2013).

[75] F. Bruneval, Phys. Rev. Lett. **108**, 256403 (2012).

[76] T. Böker, R. Severin, A. Müller, C. Janowitz, R. Manzke, D. Voß, P. Krüger, A. Mazur, and J. Pollmann, Phys. Rev. B **64**, 235305 (2001).

[77] T. J. Wieting and J. L. Verble, Phys. Rev. B **3**, 4286 (1971).

[78] A. M. Goldberg, A. R. Beal, F. A. Lvy, and E. A. Davis, Philos. Mag. **32**, 367 (1975).

[79] W. Kautek, H. Gerischer, and H. Tributsch, J. Electrochem. Soc. **127**, 2471 (1980).

[80] K. K. Kam and B. A. Parkinson, J. Phys. Chem. **86**, 463 (1982).

[81] E. Fortin and W. Sears, J. Phys. Chem. Solids **43**, 881 (1982).

[82] R. Soklaski, Y. Liang, and L. Yang, Appl. Phys. Lett. **104**, 193110 (2014).

[83] N. Peimyoo, J. Shang, C. Cong, X. Shen, X. Wu, E. K. L. Yeow, and T. Yu, ACS Nano **7**, 10985 (2013).

[84] A. Chernikov, T. C. Berkelbach, H. M. Hill, A. Rigosi, Y. Li, O. B. Aslan, D. R. Reichman, M. S. Hybertsen, and T. F. Heinz, Phys. Rev. Lett. **113**, 076802 (2014).

[85] K. He, N. Kumar, L. Zhao, Z. Wang, K. F. Mak, H. Zhao, and J. Shan, Phys. Rev. Lett. **113**, 026803 (2014).

[86] Z. Ye, T. Cao, K. O'Brien, H. Zhu, X. Yin, Y. Wang, S. G. Louie, and X. Zhang, Nature (London) **513**, 214 (2014).

[87] C. Zhang, A. Johnson, C.-L. Hsu, L.-J. Li, and C.-K. Shih, Nano Lett. **14**, 2443 (2014).

[88] Y. Lin, X. Ling, L. Yu, S. Huang, A. L. Hsu, Y.-H. Lee, J. Kong, M. S. Dresselhaus, and T. Palacios, Nano Lett. **14**, 5569 (2014).

[89] H.-P. Komsa and A. V. Krasheninnikov, Phys. Rev. B **86**, 241201 (2012).

[90] F. Hüser, T. Olsen, and K. S. Thygesen, Phys. Rev. B **88**, 245309 (2013).

[91] D. Y. Qiu, F. H. da Jornada, and S. G. Louie, Phys. Rev. Lett. **111**, 216805 (2013).

[92] S. B. Zhang and J. E. Northrup, Phys. Rev. Lett. **67**, 2339 (1991).

[93] K. Reuter and M. Scheffler, Phys. Rev. B **65**, 035406 (2001).

[94] C. G. Van de Walle and J. Neugebauer, J. Appl. Phys. **95**, 3851 (2004).
[95] C. Freysoldt, B. Grabowski, T. Hickel, J. Neugebauer, G. Kresse, A. Janotti, and C. G. Van de Walle, Rev. Mod. Phys. **86**, 253 (2014).
[96] H.-P. Komsa, T. T. Rantala, and A. Pasquarello, Phys. Rev. B **86**, 045112 (2012).
[97] M. W. J. Chase, *NIST-JANAF Thermochemical Tables*, 4th ed. (American Institute of Physics, New York, 1998).
[98] P. J. Linstrom and W. G. Mallard, eds., *NIST Chemistry WebBook, NIST Standard Reference Database Number 69* (National Institute of Standards and Technology, Gaithersburg, MD), http://webbook.nist.gov.
[99] P. Raybaud, J. Hafner, G. Kresse, S. Kasztelan, and H. Toulhoat, J. Catal. **189**, 129 (2000).
[100] H. Schweiger, P. Raybaud, G. Kresse, and H. Toulhoat, J. Catal. **207**, 76 (2002).
[101] M. V. Bollinger, K. W. Jacobsen, and J. K. Nørskov, Phys. Rev. B **67**, 085410 (2003).
[102] D. Alfè, Comput. Phys. Commun. **180**, 2622 (2009).
[103] D. R. Lide, ed., *CRC Handbook of Chemistry and Physics, Internet Version* (CRC Press, Boca Raton, FL, 2005).
[104] M. Leslie and M. J. Gillan, J. Phys. C: Solid State Phys. **18**, 973 (1985).
[105] G. Makov and M. C. Payne, Phys. Rev. B **51**, 4014 (1995).
[106] C. Freysoldt, J. Neugebauer, and C. G. Van de Walle, Phys. Rev. Lett. **102**, 016402 (2009).
[107] H.-P. Komsa and A. Pasquarello, Phys. Rev. Lett. **110**, 095505 (2013).
[108] R. Rurali and X. Cartoixa, Nano Lett. **9**, 975 (2009).
[109] Y. Kumagai and F. Oba, Phys. Rev. B **89**, 195205 (2014).
[110] H.-P. Komsa, N. Berseneva, A. V. Krasheninnikov, and R. M. Nieminen, Phys. Rev. X **4**, 031044 (2014).
[111] A. Carvalho and A. H. Castro Neto, Phys. Rev. B **89**, 081406 (2014).
[112] J.-Y. Noh, H. Kim, and Y.-S. Kim, Phys. Rev. B **89**, 205417 (2014).
[113] A. Alkauskas, P. Broqvist, and A. Pasquarello, Phys. Rev. Lett. **101**, 046405 (2008).
[114] H.-P. Komsa, P. Broqvist, and A. Pasquarello, Phys. Rev. B **81**, 205118 (2010).
[115] W. Chen and A. Pasquarello, Phys. Rev. B **86**, 035134 (2012).
[116] W. Chen and A. Pasquarello, Phys. Rev. B **88**, 119906(E) (2013).
[117] L. Wirtz, A. Marini, and A. Rubio, Phys. Rev. Lett. **96**, 126104 (2006).
[118] R. Schlaf, O. Lang, C. Pettenkofer, and W. Jaegermann, J. Appl. Phys. **85**, 2732 (1999).
[119] Y.-H. Chang, W. Zhang, Y. Zhu, Y. Han, J. Pu, J.-K. Chang, W.-T. Hsu, J.-K. Huang, C.-L. Hsu, M.-H. Chiu, T. Takenobu, H. Li, C.-I. Wu, W.-H. Chang, A. T. S. Wee, and L.-J. Li, ACS Nano **8**, 8582 (2014).
[120] M.-L. Tsai, S.-H. Su, J.-K. Chang, D.-S. Tsai, C.-H. Chen, C.-I. Wu, L.-J. Li, L.-J. Chen, and J.-H. He, ACS Nano **8**, 8317 (2014).
[121] C. Ataca and S. Ciraci, J. Phys. Chem. C **115**, 13303 (2011).
[122] S. KC, R. C. Longo, R. Addou, R. M. Wallace, and K. Cho, Nanotechnology **25**, 375703 (2014).
[123] J. C. Caulfield and A. J. Fisher, J. Phys.: Condens. Matter **9**, 3671 (1997).
[124] J. D. Fuhr, A. Saúl, and J. O. Sofo, Phys. Rev. Lett. **92**, 026802 (2004).
[125] D. Liu, Y. Guo, L. Fang, and J. Robertson, Appl. Phys. Lett. **103**, 183113 (2013).
[126] K. S. Yong, D. M. Otalvaro, I. Duchemin, M. Saeys, and C. Joachim, Phys. Rev. B **77**, 205429 (2008).
[127] H.-P. Komsa, S. Kurasch, O. Lehtinen, U. Kaiser, and A. V. Krasheninnikov, Phys. Rev. B **88**, 035301 (2013).
[128] D. Le, T. B. Rawal, and T. S. Rahman, J. Phys. Chem. C **118**, 5346 (2014).
[129] X. Zou, Y. Liu, and B. I. Yakobson, Nano Lett. **13**, 253 (2013).
[130] A. Earnshaw and N. Greenwood, *Chemistry of the Elements*, 2nd ed. (Elsevier, Amsterdam, 1997).
[131] L. Yadgarov, R. Rosentsveig, G. Leitus, A. Albu-Yaron, A. Moshkovich, V. Perfilyev, R. Vasic, A. I. Frenkel, A. N. Enyashin, G. Seifert, L. Rapoport, and R. Tenne, Angew. Chem. Int. Ed. **51**, 1148 (2012).
[132] Y.-C. Lin, D. O. Dumcenco, H.-P. Komsa, Y. Niimi, A. V. Krasheninnikov, Y.-S. Huang, and K. Suenaga, Adv. Mater. **26**, 2857 (2014).
[133] B. Sachs, L. Britnell, T. O. Wehling, A. Eckmann, R. Jalil, B. D. Belle, A. I. Lichtenstein, M. I. Katsnelson, and K. S. Novoselov, Appl. Phys. Lett. **103**, 251607 (2013).
[134] G. Zhang, A. Canning, N. Grønbech-Jensen, S. Derenzo, and L.-W. Wang, Phys. Rev. Lett. **110**, 166404 (2013).
[135] Q. C. Sun, L. Yadgarov, R. Rosentsveig, G. Seifert, R. Tenne, and J. L. Musfeldt, ACS Nano **7**, 3506 (2013).
[136] C. H. Ho, C. S. Wu, Y. S. Huang, P. C. Liao, and K. K. Tiong, J. Phys.: Condens. Matter **10**, 9317 (1998).
[137] Y. J. Wu, P. H. Wu, J. Jadczak, Y. S. Huang, C. H. Ho, H. P. Hsu, and K. K. Tiong, J. Appl. Phys. **115**, 223508 (2014).
[138] S. H. El-Mahalawy and B. L. Evans, J. Appl. Crystallogr. **9**, 403 (1976).
[139] C. Sevik, Phys. Rev. B **89**, 035422 (2014).
[140] D. Çakir, F. M. Peeters, and C. Sevik, Appl. Phys. Lett. **104**, 203110 (2014).
[141] P. Erhart and K. Albe, J. Appl. Phys. **104**, 044315 (2008).
[142] A. Ramasubramaniam, Phys. Rev. B **86**, 115409 (2012).
[143] H. Peelaers and C. G. Van de Walle, Phys. Rev. B **86**, 241401 (2012).
[144] A. Glensk, B. Grabowski, T. Hickel, and J. Neugebauer, Phys. Rev. X **4**, 011018 (2014).